Active Hyperspectral Imaging of Chemicals on Surfaces

by

Travis R. Myers

B.S. Mathematics and Materials Chemistry
United States Air Force Academy, 2012

SUBMITTED TO THE DEPARTMENT OF MATERIALS SCIENCE AND ENGINEERING IN PARTIAL FULFILLMENT OF THE REQUIREMENTS FOR THE DEGREE OF

MASTER OF SCIENCE IN MATERIALS SCIENCE
AT THE
MASSACHUSETTS INSTITUTE OF TECHNOLOGY

SEPTEMBER 2014

Signature of Author: .....

Department of Materials Science and Engineering
August 15, 2014

Certified by: .....

Linn Hobbs
Professor of Materials
Thesis Reader

Accepted by: .....

Gerbrand Ceder
Chair, Departmental Committee on Graduate Students

Active Hyperspectral Imaging of Chemicals on Surfaces

by
Travis Myers

Submitted to the Department of Materials Science and Engineering August 15, 2014 in Partial fulfillment of the requirements for the Degree of Master of Science in Materials Science

ABSTRACT

Active hyperspectral imaging (HSI) is a promising technique for the detection of chemicals at standoff distances. In active HSI, a target is illuminated by a laser source at many different wavelengths and a camera obtains an image of the illuminated scene at each wavelength. In this research, the feasibility of hyperspectral imaging for the detection of particles on surfaces was demonstrated using potassium chlorate particles on car panels at distances of 5 m, 10 m, and 20 m. Using the Adaptive Cosine Estimation (ACE) algorithm which compares the observed reflectance spectra to a reference spectrum, potassium chlorate fingerprints are easily visible at many different sample angles. However, in general, there is a large amount of variation in the shape and magnitude of spectra in a hyperspectral image that depend on factors such as particle size, viewing geometry, and surface reflectivity. Thus, Mie Theory calculations are performed on simulated materials and combined with information from sources such as Hapke [4], [20] to give qualitative insight into the expected shape and magnitude of reflectance spectra from sparse particles on a surface. The shape of the spectra depends on whether the particles are strongly absorbing or weakly absorbing. Strongly absorbing particles tend to have reflectance maxima near the resonant frequency, whereas weakly absorbing particles tend to have reflectance minima. For highly reflective substrates, the reflectance decreases sharply as the sample angle increases and becomes dominated by backward scattering from the particle which has a flatter spectrum around the Christiansen frequency, the frequency at which the refractive index of the particle is closest to one. The double interaction model, which uses Mie Theory to calculate the contributions to the reflectance along two different light paths, is used to accurately account for how the shape and magnitude of the reflectance spectra of sodium chlorate particles on gold and silica surfaces changes as a function of sample angle and laser angle. A method for approximating the mean particle size based on the location of the peak near the Christiansen frequency is derived. This method, when applied to the sodium chlorate sample, yields a result for the mean particle diameter that is approximately half of the value determined using a microscope.

The Hapke Isotropic Multiple Scattering Approximation (IMSA), combined with Mie Theory, is used to give qualitative insight into the expected shape and magnitude of reflectance spectra from bulk powders. Compared with the reflectance spectra from sparse particles, the spectra from bulk powders are much simpler and less dependent on the viewing geometry. The Hapke IMSA model is able to accurately account for the observed changes in the reflectance from bulk sodium chlorate powder at multiple sample angles and laser angles.

A final scenario of interest is thin films on rough or porous surfaces. Using a model that takes into account diffusely reflected and specularly reflected light, the observed reflectance spectra from diethyl phthalate (DEP) on a brick is fitted to a high degree of accuracy. This suggests a promising method for using hyperspectral imaging to determine the thickness of liquids on porous surfaces.

Finally, the issue of speckle in hyperspectral imaging was examined using simulations based on Fourier optics and information from sources such as Goodman [6], [17]. Speckle is a limiting factor in hyperspectral imaging because it is noise that scales with the signal, and thus cannot be eliminated by increasing the signal strength. Equations from various sources are presented that describe the reduction in speckle contrast for spatial, spectral, polarization, temporal, and angular averaging. Original equations for the reduction in contrast for spectral and angular averaging are derived.

Thesis Reader: Linn Hobbs
Title: Professor of Materials

Acknowledgements

First of all, I would like to thank my research advisor Anish Goyal for his patience, expert guidance, and enlightening discussions. I would also like to thank my other research advisor Antonio Sanchez-Rubio and my thesis reader Linn Hobbs. Finally, thanks to Bill Herzog, Daniel Ripin, T.Y. Fan, and everyone else in Group 82 at MIT Lincoln Laboratory, which supported this research.

Contents

List of Figures

Introduction

In active hyperspectral imaging, a scene is illuminated by a laser source at many different wavelengths and the reflected light is imaged with a camera at each wavelength, resulting in a reflectance spectrum for every pixel in the image. This technique enables chemical mapping of the scene by using a suitable detection algorithm to compare the reflectance spectrum in each pixel to a reference spectrum for any chemical of interest. However, a major obstacle to practical chemical imaging is the fact that the observed reflectance for a particular chemical has a significant amount of variability. This variability arises primarily from two sources: 1) variability in the intensity of the reflectance due to factors such as particle size and shape, surface reflectivity, and viewing geometry, and 2) variability due to coherent interference of light in a process known as speckle. Both of these sources of variability were analyzed by using models to simulate the expected spectra in different scenarios and then comparing the simulated results with controlled experiments. By understanding how the spectra change in different circumstances, one can mitigate the negative impacts of this variability on the detection of a chemical of interest.

An important application of active hyperspectral imaging is the detection of trace amounts of explosive residue. There have been previous efforts at understanding the reflectance spectra of explosives for this purpose ([16], [21], [25], [27], [15]). Much of the current literature on this subject focuses on the phenomenon of "contrast reversal", whereby valleys in the transmittance spectrum of a material show up as peaks in the reflectance spectrum when the material is placed on an absorbing substrate. In Reference [1], for instance, the authors measured the specular reflectance of thin films of TNT of varying thicknesses on an aluminum substrate and on a painted car panel. It was found that the spectra from the aluminum substrate closely matched the FTIR transmittance spectrum of TNT, but the spectra from the painted car panel showed contrast reversal for samples with large thicknesses. This effect is explained in Chapter 4. In any case, the particular scenario studied by the authors is of limited interest because in most real-world scenarios, the detector will not be specularly aligned with the illumination source. The authors in Reference [2] performed reflectance measurements under more realistic conditions: they measured the backscattered light of PETN and TNT fingerprints on a painted car panel near normal

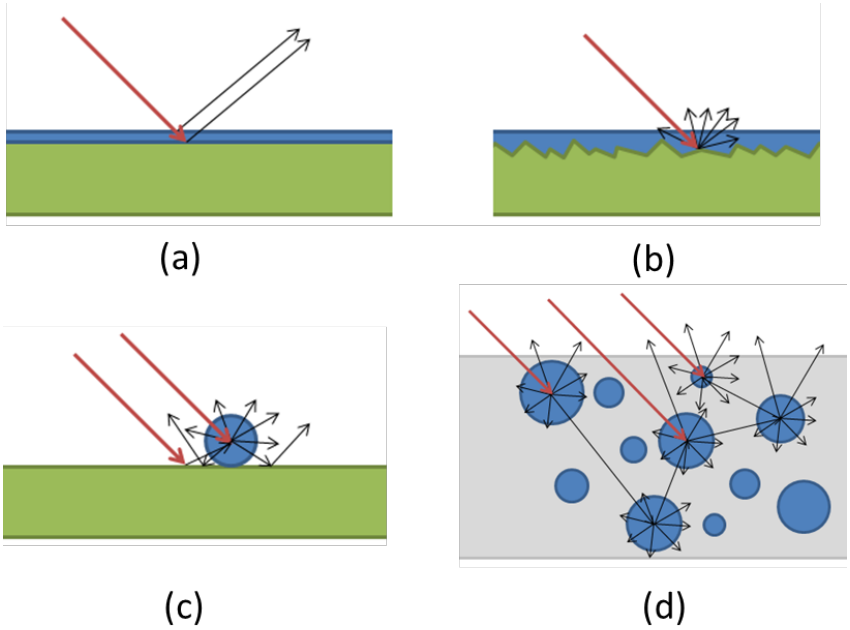

Figure 1: Reflectance scenarios of interest. (a) thin film on smooth surface; (b) thin film on rough surface; (c) sparse particles on a smooth surface; and (d) bulk powders.

incidence. For PETN, they found that the reflectance spectrum was transmittance-like in some parts of the spectrum and displayed contrast reversal in other parts. For TNT, the observed reflectance spectrum was even more complicated. They noted that "a full theoretical description of the expected spectra will be very difficult." Chapter 2 makes an effort in this direction for simulated materials that have refractive indices similar to explosives such as TNT and PETN.

The viewing geometry with respect to the surface can have a considerable effect on the shape and magnitude of the reflectance spectra. In Reference [3], the reflectance spectrum as a function of sample angle was measured for TNT, RDX, and tetryl on a car door panel. The authors concluded from their study that

> this data supports the need for a detailed empirical and theoretical study to improve the understanding of diffuse reflectance from materials having different particle morphologies deposited upon a variety of substrates under different measurement geometries.

This thesis, partially drawing from previously published works [18] and [19], is a step towards this goal. Figure shows the various scenarios for reflectance that will be explored: (a) specular reflectance from a film on a smooth surface (Chapter 4); (b) reflectance from a film on a rough surface (Chapter 4); (c) reflectance from particles on a smooth surface (Chapter 2); and (d) reflectance from bulk collections of particles (Chapter 3).

Chapter 1 presents an overview of active hyperspectral imaging in the long-wave infrared (LWIR) and describes the experimental methods that were used in this research. In particular, since the laser output and the signal response of the camera vary with wavelength, it is important to employ a suitable normalization method in order to extract a consistent reflectance spectrum. Also described is the definition of the bidirectional reflectance distribution function (BRDF), which is commonly used for describing the scattering of light by a surface, and the Adaptive Cosine Estimation (ACE) detection algorithm. A demonstration of standoff detection of potassium chlorate on a car panel is given as an example. Chapter 2 considers the reflectance spectra from sparse particles on a smooth surface. The magnitude and shape of the observed reflectance spectrum depend on the particle size distribution, the reflectivity of the surface, and the viewing geometry relative to the surface. The shape of the reflectance spectra are qualitatively different for strongly absorbing materials and weakly absorbing materials. The models are validated by comparison with an experiment with sodium chlorate. In Chapter 3, the same simulated materials are used to gain an understanding of the reflectance from bulk powders using a model developed by Hapke. Once again, the results are tested by experiment with sodium chlorate powder. Chapter 4 considers the reflectance from thin films on smooth surfaces, rough surfaces, and porous surfaces. Finally, in Chapter 5 explore the effects of speckle on hyperspectral imaging and the various ways in which the effects can be mitigated.

Symbols and Definitions

A: total absorption coefficient in a particulate medium (i.e., the inverse of the distance light must travel to decrease in intensity by a factor of e due to absorption).

c: speed of light in vacuum.

C: speckle contrast.

d: distance between camera and sample.

D: particle diameter or film thickness.

f: focal length of the camera.

k: imaginary part of the refractive index.

I: intensity.

L: radiance.

M: degrees of freedom parameter in regard to speckle.

n: real part of the refractive index.

N: complex refractive index.

$p(g)$: phase function which describes scattering intensity as a function of g, the angle between the scattering direction and the incident direction.

Q_A: absorption efficiency, the ratio of the light absorbed by a particle to the light incident on its cross section.

Q_E: extinction efficiency, the ratio of the total light either scattered or absorbed by a particle to the light incident on its cross section.

Q_S: scattering efficiency, the ratio of the light scattered by a particle to the light incident on its cross section.

R: reflectance (BRDF).

r: reflectance amplitude.

$\mathcal{R}$: ratio of pixel area to speckle correlation area.

S: total scattering coefficient in a particulate medium (i.e., the inverse of the distance light must travel to decrease in intensity by a factor of e due to scattering).

T: camera integration time.

u: the tangent of the observation/sample angle.

v: velocity.

w: single-scatter albedo, equal to absorption efficiency divided by extinction efficiency.

α: absorption coefficient, equal to $4\pi k\widetilde{\nu}$.

ϵ: complex permittivity.

ϵ': real part of the permittivity.

ϵ'': imaginary part of the permittivity.

λ: wavelength.

Λ: the triangle function.

ω: angular frequency.

Ω: solid angle.

ρ: correlation of speckle patterns.

ν: frequency.

θ_I: angle of incidence, the angle between the laser propagation direction and the surface normal of the sample.

θ_L: laser angle, the angle between the laser propagation direction and the camera axis.

θ_E: emittance angle (or sample angle), the angle between the surface normal of the sample and the emitted light detected by the camera.

$\widetilde{\nu}$: spectral wavenumber, the inverse of the wavelength of light in vacuum.

BRDF: bidirectional reflectance distribution function, the ratio of the reflected radiance to the incident intensity.

Emittance Angle: the angle of the scattered light relative to the surface normal.

GSD: ground sample distance, the width of a pixel projected into the object plane.

Reflectance Spectrum: the reflectance as a function of wavenumber or wavelength.

Resolution Cell: the smallest region in the imaging plane that can be resolved.

Projected Resolution Cell: the resolution cell projected into the object plane.

Scattering Plane: the plane containing the incident laser direction and the scattering direction.

Chapter 1

Hyperspectral Imaging Concepts and Demonstrations

1.1 Overview

In hyperspectral imaging, a scene is imaged at many different wavelengths to provide spectral information for every pixel within the scene. Active imaging means that the scene is illuminated by an active source such as a laser, rather than a passive source such as the sun or blackbody thermal radiation. Active imaging enables a much greater signal to noise ratio than passive imaging.

The mid-infrared (MIR) region of the electromagnetic spectrum covers wavelengths from approximately $3\,\mu$m to $15\,\mu$m. The long wave infrared (LWIR) is the portion of the MIR region with wavelengths between approximately $8\,\mu$m and $15\,\mu$m. The LWIR region is ideal for chemical imaging because many chemicals have unique spectral signatures in this wavelength range The LWIR region is one of the atmospheric windows, which are regions of the electromagnetic spectrum which can be transmitted through the atmosphere with very little absorption. Active HSI in the long wave infrared (LWIR)has been enabled by the development of quantum cascade lasers (QCL's), which allow tuning over a broad range of wavelengths. QCL's are a game-changer in MIR laser technology because they are compact, efficient, reliable, and provide continuous wavelength coverage over much of the MIR range with high power and good beam quality while operating room temperature.

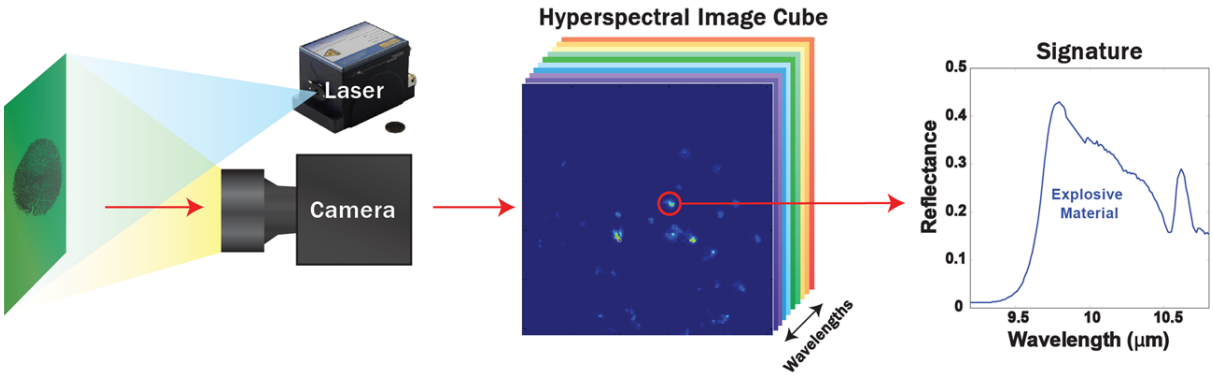

Figure 1.1: The hyperspectral imaging process. A sample is illuminated by a laser, and the reflected light is captured by a camera. Images from many different wavelengths are processed to produce a reflectance spectrum under each pixel of the hyperspectral image cube.

1.2 Equipment and Experimental Setup

The basic features of active hyperspectral imaging are shown in 1.1. The sample is illuminated by a laser source at one wavelength and an image of the scene is obtained by the camera. This process is repeated for many different wavelengths in the spectral region of interest to create a hypercube. For most of the research, the illumination was provided by two Daylight Solutions lasers which together spanned a wavelength range of $9 - 11\,\mu$m. The sample was typically illuminated with a circular beam a few centimeters in diameter. The camera used in this research was a digital focal plane array (DFPA) composed of 256x256 30-μm-pixels with an analog to digital converter under each pixel.

The DFPA has the ability to switch very rapidly from a count-up mode to a count-down mode, allowing for on-chip background substraction. The advantage of background subtraction is demonstrated in Figure 1.2. An external pulser was used to synchronize the laser pulse and the DFPA integration times. The total integration time of the DFPA was $100\,\mu$s. Figure 1.2(a) shows the result of conventional imaging, in which the DFPA counts up for the full $100\mu s$ during a single laser pulse. It is virtually impossible to detect the reflectance of the laser on the hand. Figure 1.2(b) demonstrates the advantage of synchronous imaging, in which the DFPA is synchronized with the laser pulse so that it counts up for $2\,\mu$s during each $0.5\,\mu$s laser pulse. This process is repeated 50 times. The reflectance from the laser is now barely visible. Finally, Figure 1.2(c) demonstrates synchronous imaging with background subtraction in which the DFPA counts up for $2\,\mu$s while the laser is on and counts down for $2\,\mu$s while the laser is off. The laser reflectance is now very clear because the contribution of the passive thermal background has been subtracted, yielding only the active return.

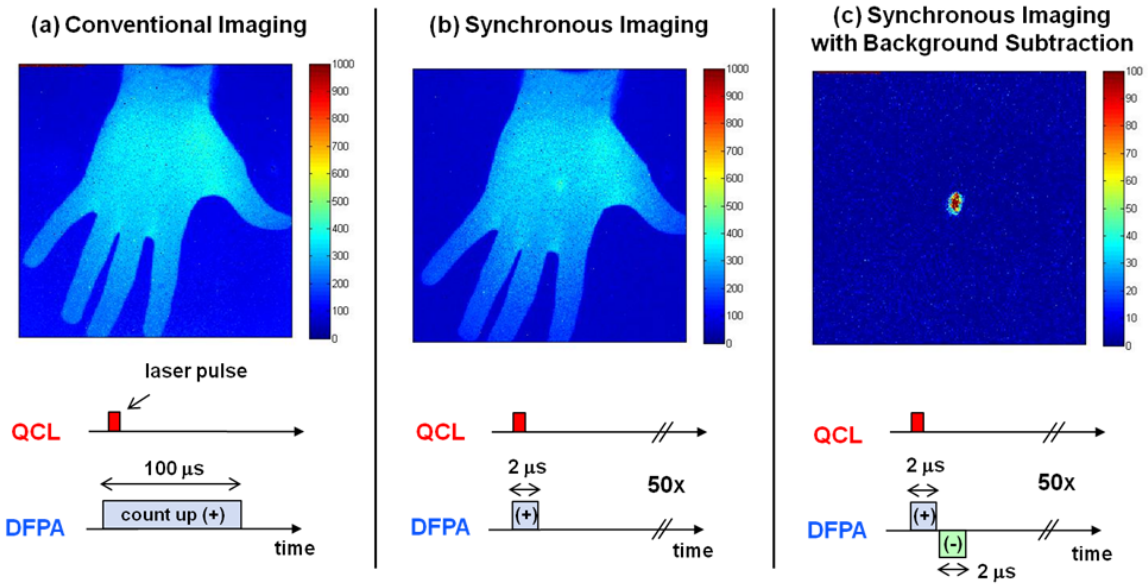

Figure 1.2: A demonstration of the advantages of synchronous imaging and background subtraction.

1.3 Reflectance Spectra and Normalization Methods

There are many definitions of reflectance [4]. In this thesis, I will use the definition of the Bidirectional Reflectance Distribution Function (BRDF) as given by Hapke. In terms of parameters relevant to hyperspectral imaging, the BRDF is given by

$$r = \frac{L}{I} = \frac{P_{pixel}}{I(GSD)^2\Omega}, \tag{1.1}$$

where L is the radiance in the emitted direction, I is the intensity of the laser (power per unit area normal to the propagation direction), P_{pixel} is the power received at the pixel, GSD is the ground sample distance (the width of a pixel projected onto the object plane), and Ω is the solid angle of the aperture. For a given sample, the BRDF is a function of the laser angle (θ_L), emittance angle (θ_E), and angle of incidence (θ_I). These angles are shown in Figure 1.3. The laser angle is the angle between the laser propagation direction and the DFPA axis; the emittance angle is the angle between the surface normal of the sample and the DFPA axis; and the angle of incidence is the angle between the laser propagation direction and the surface normal. Note that the laser propagation direction, DFPA axis, and surface normal do not necessarily lie in the same plane.

The BRDF has units of inverse steradians. The BRDF of a perfectly reflecting Lambertian surface is $\frac{\cos\theta_I}{\pi}$.

In this thesis, I use the terms "reflectance" and "BRDF" almost interchangeably, except that graphs

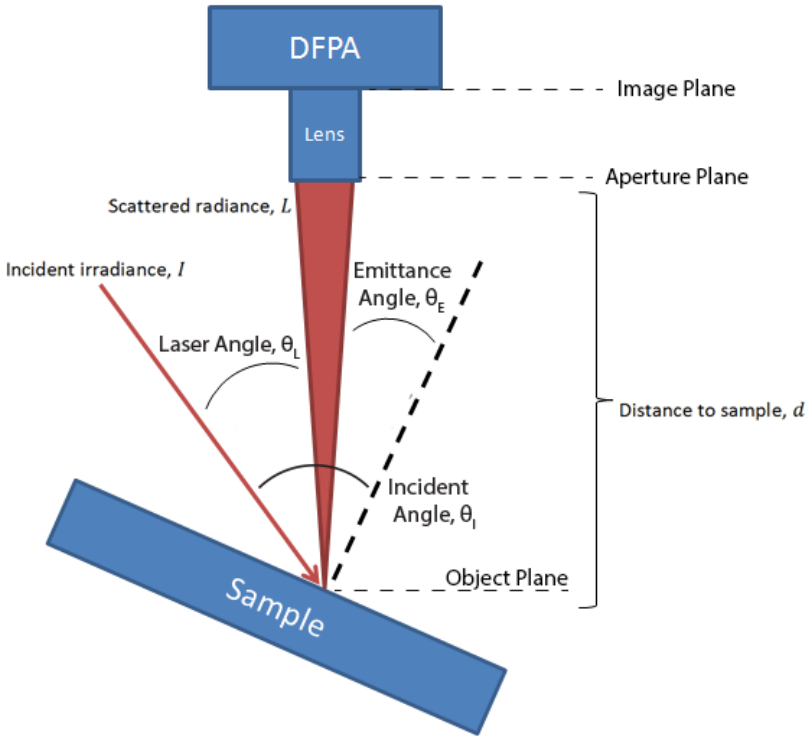

Figure 1.3: Geometry Definitions.

labeled "reflectance" may be in arbitrary units; that is, they may be scaled relative to the actual BRDF. Graphs labeled "BRDF" represent the actual BRDF as calculated using Equation 1.1. Also, when discussing specular reflection, the term "reflectance" simply refers to the ratio of reflected light to incident light. The term "reflectance spectrum" refers to the reflectance (BRDF) as a function of wavelength or wavenumber.

When making measurements of the reflectance of a sample, it is necessary to normalize the observed reflectance to some standard because the intensity of the laser and the camera detection sensitivity are not constant across all wavelengths. In this research, a hyperspectral image of a diffusely reflecting gold standard was used in the same location and orientation as the sample. If the gold standard were an ideal Lambertian reflector and each pixel in the hyperspectral image perfectly represented the reflectance of the gold standard, then one could just divide each pixel of the sample hyperspectral image by each pixel of the gold standard hyperspectral image to yield a hyperspectral image representing the (scaled) BRDF at every wavelength. Unfortunately, the gold standard is not perfectly Lambertian, and because of speckle (discussed in Chapter 5) and/or surface irregularities in the gold standard, each pixel does not perfectly represent the reflectance of the gold standard (at close distance, surface irregularities become a problem while at long distance, speckle becomes a problem). To solve the problem due to speckle/surface

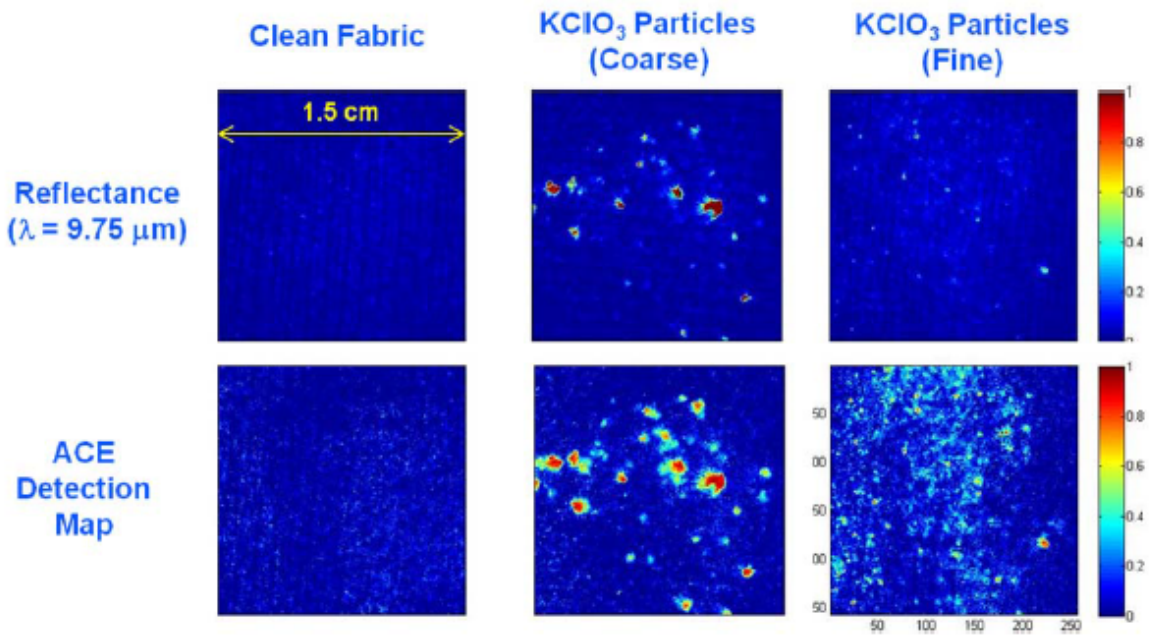

Figure 1.4: Examples of ACE detection maps of potassium chlorate particles on fabric.

irregularities, one can average over a sufficient number of pixels to smooth out the variation. To solve the problem of the gold standard not being perfectly Lambertian, one can sacrifice knowledge of the absolute BRDF in order to obtain reflectance measurements that are in the correct proportion to one another by setting the sum of all the illuminated pixels in the gold standard equal to the same constant for each illumination wavelength. To obtain the actual BRDF, one could directly measure the laser power in terms of DFPA counts, but this measurement turned out to be difficult in practice.

1.4 Detection Maps

Once the hyperspectral image is obtained, the goal is to identify the chemicals that are present in the scene by comparing the reflectance spectrum in each pixel to a reference spectrum. The primary algorithm used in this research for this purpose is the Adaptive Cosine Estimation (ACE) algorithm. This algorithm is described in Reference [5]. This algorithm uses the statistics of the background clutter as an input. Portions of the scene which are known to not contain the chemical of interest can often be used to obtain background clutter statistics. Figure 1.4 shows examples of detection maps of potassium chlorate particles on a fabric. The top row shows the reflectance at a wavelength of 9.75 μm, and the bottom row shows the resulting ACE detection map. The clean fabric shows very low detection values whereas both the coarse and fine particles have high detection values as expected.

1.5 Demonstration: Standofff ACE Detection of Potassium Chlorate Fingerprints

In order to demonstrate hyperspectral imaging at standoff distances, a sample consisting of a potassium chlorate fingerprint on a car panel was imaged at distances of 5 m, 10 m, and 20 m using a lens with a 200 mm focal length. The laser was pulsed at 2.5 kHz with a pulse width of 0.5 μs. The DFPA counted up for 4 μs beginning 0.3 μs before each laser pulse and counted down for 4 μs beginning 6 μs after the count up was completed. Each DFPA frame contained 50 count-up/count-down cycles and 128 frames were averaged at each wavelength. The first laser operated at wavenumbers 926 cm^{-1} through 1004 cm^{-1} in 1 cm^{-1} steps, and the second laser operated at wavenumbers 1017 cm^{-1} through 1100 cm^{-1} in 1 cm^{-1} steps for a total of 164 different wavelengths in each hyperspectral image cube.

At each distance, the sample was mounted vertically and rotated at angles of 5°, 15°, 30°, and 45° around the vertical axis. The diffuse gold standard was also imaged once at each distance. A reflectance spectrum was taken from the gold standard by averaging over many pixels in the hyperspectral image, and the hyperspectral images of the samples were normalized by dividing each pixel by the reflectance spectrum of the diffuse gold standard. ACE detection maps were obtained by using an unilluminated part of each image as the background clutter (this amounts to assuming that the background spectra is noise).

The detection maps at 5 m range are shown in Figure 1.5. The potassium chlorate fingerprint is clearly distinguished from the background. Figure 1.6 shows the ACE detection maps at 10 m. The detection is nearly as good as at 5 m. In the absence of speckle, one would expect that the detection ability would not depend on distance because the signal to noise ratio is independent of the distance. The reason for this is that even though the total power received by the camera decreases with the square of the distance, the number of illuminated pixels also decreases by the same proportion, so the power received by each pixel remains the same. Figure 1.7 shows the detection maps at 20 m. The strength of the detection is significantly lower than at 20 m, possibly due to the effect of speckle. As will be explained in Chapter 5, the spectral correlation length decreases in proportion to the distance to the object, and thus the number of fluctuation peaks in the spectra due to speckle doubles from 5 m to 10 m and from 10 m to 20 m.

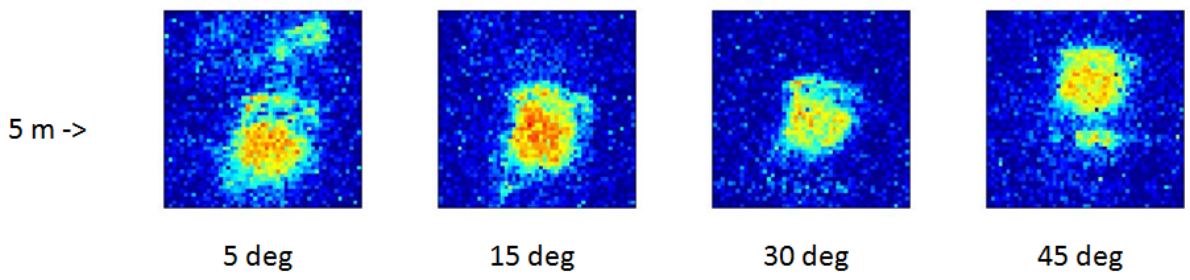

Figure 1.5: ACE maps of $KClO_3$ fingerprints on a car panel at 5m.

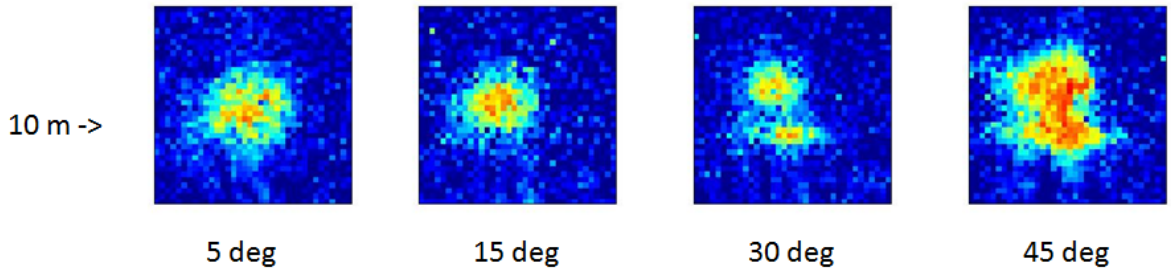

Figure 1.6: ACE maps of $KClO_3$ fingerprints on a car panel at 10m.

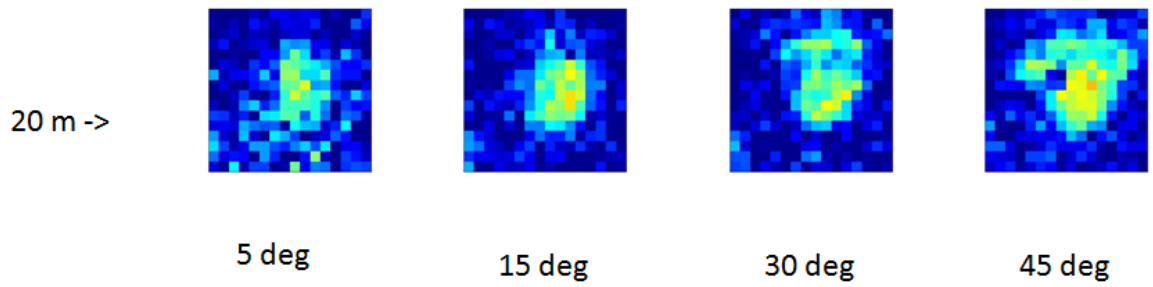

Figure 1.7: ACE maps of $KClO_3$ fingerprints on a car panel at 20m.

Chapter 2

Reflectance Spectra of Solid Particles on Smooth Surfaces

2.1 Overview

In this chapter, Mie Theory is used to model the reflectance from sparse solid particles on a smooth surface (as in, for example, fingerprints on a car panel). I explore how the intensity and shape of the reflectance spectrum depends on particle size, viewing geometry, substrate reflectance, and the absorption strength of the particle. To enable a simplified analysis, the reflectance spectra from two simulated materials are calculated. The results predicted by the model are then compared with experimental data of sodium chlorate particles on gold and silica surfaces.

2.2 Simulated Materials

Absorption features of dielectric materials can be understood using the Lorentz model which treats the material as being composed of an ensemble of damped harmonic oscillators with various resonance frequencies. The imaginary part of the permittivity of the material is a Lorentzian function centered around the resonance frequency. The complex permittivity as a function of wavenumber is

$$\epsilon(\widetilde{\nu}) = n_{\infty}^2 + \sum_i \frac{S_i \gamma_i \widetilde{\nu}}{\widetilde{\nu}_{0,i}^2 - \widetilde{\nu}^2 - i\gamma_i \widetilde{\nu}}, \tag{2.1}$$

where n_∞ is the refractive index at $\widetilde{\nu} = \infty$, $\widetilde{\nu}_0$ is the resonant wavenumber, S is the magnitude of the imaginary part of the permittivity when $\nu = \nu_0$, and γ is the damping coefficient (equal to the full

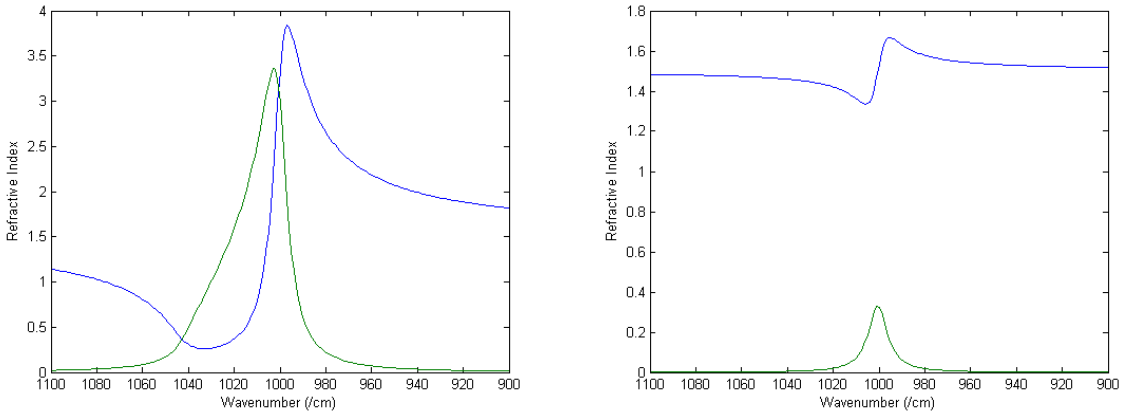

Figure 2.1: Refractive indices of simulated materials. Material 1 (left) is strongly absorbing and Material 2 (right) is weakly absorbing.

width at half maximum of the imaginary part of the permittivity). The complex refractive index is the square root of the complex permittivity:

$$N = \sqrt{\epsilon}. \tag{2.2}$$

In this chapter, two simulated materials will be examined. Material 1 is strongly absorbing (S is large) and Material 2 is weakly absorbing (S is small). Strong absorption features are typical of explosive materials such as potassium chlorate, sodium chlorate, or ammonium nitrate. Weak absorption features are typical of explosives materials such as TNT or RDX. The refractive index of some of these explosive materials are shown in Figure 2.2.

Both simulated materials have imaginary permittivity peaks centered at $1000\,\mathrm{cm}^{-1}$ with a full-width-half-max (FWHM) of $10\,\mathrm{cm}^{-1}$ and refractive index at infinity of 1.5. The peak height of the imaginary part of the permittivity for Material 1 is 20, and for Material 2 the peak height is 1. The refractive indices of these materials as a function of wavenumber are shown in Figure 2.1.

2.3 Reflectance Spectra of Isolated Spherical Particles

In this section, the reflectance spectra of isolated particles is calculated using Mie Theory which gives the exact solution for the scattering of plane waves by spherical particles ([**?**], [8], [14]). With some qualifications which are discussed in the next section, Mie Theory serves as a good foundation for understanding the reflectance of non-spherical particles for which electromagnetic scattering calculations are difficult. For the Mie Theory calculations in this thesis, Matlab programs written by Christian Matzler were used ([7]). The Matlab code used to calculate the BRDF for a distribution of particles

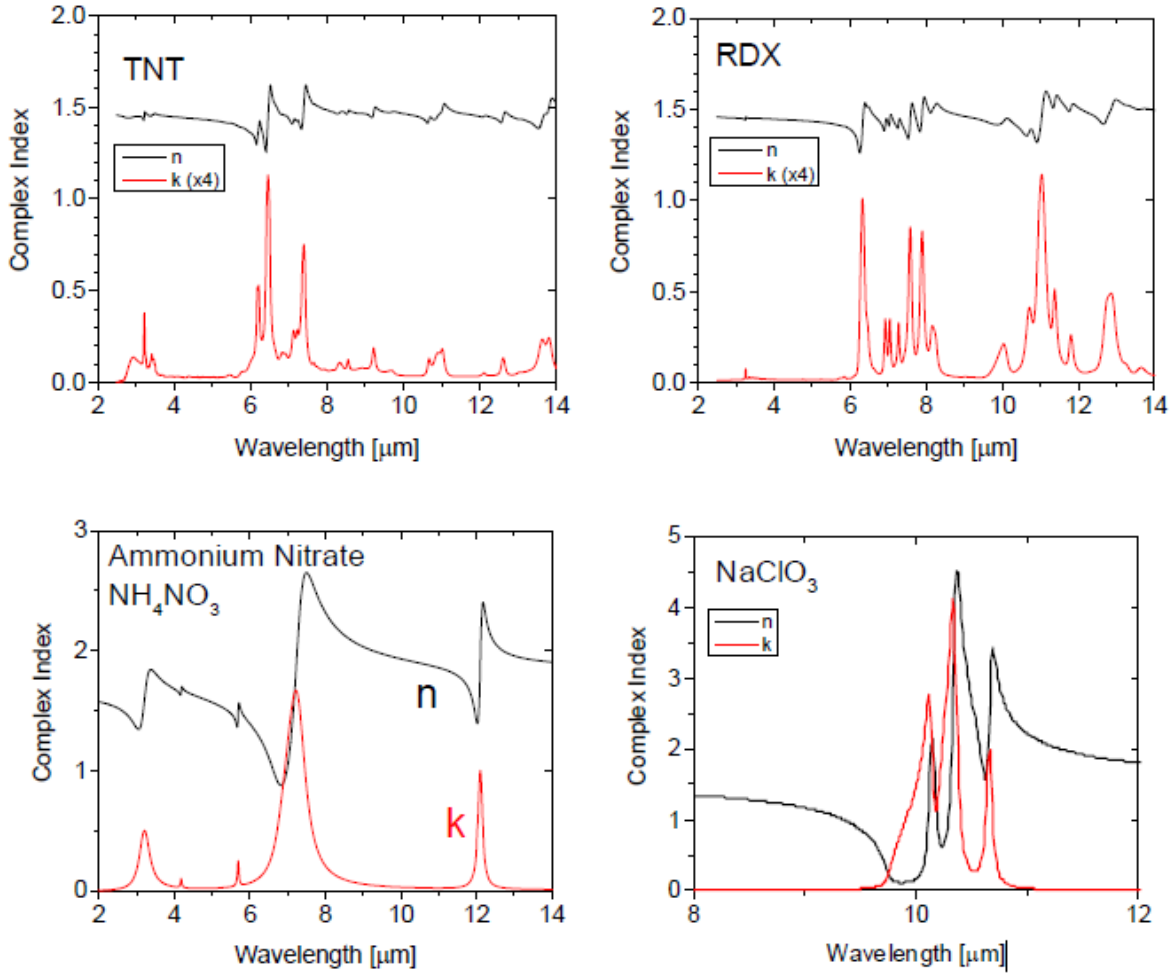

Figure 2.2: Refractive indices of various explosives.

using Matzler's functions is given in Appendix A.1

Figure 2.3 shows the calculated reflectance spectra for the two simulated materials described in Section 2.2. The blue curve is Material 1, the green curve is Material 2, and the light gray curve is a material with no absorption feature and a constant refractive of 1.5. The left half of the figure shows "reflectance" at an angle of 10° from the laser propagation direction (i.e., forward scattering), and the right half of the figure shows reflectance at an angle of 170° from the laser propagation direction (i.e., backscattering). In these calculations, it is assumed that the polarization is perpendicular to the scattering plane. When the deviation from directly forward or directly backward scattering is small, the polarization is not a significant factor. When the angle between the propagation direction and the scattered direction is large, the scattering intensity can be significantly smaller when the polarization is parallel to the scattering plane; for example, in the Rayleigh limit, the scattered intensity at 90° to the propagation direction is zero.

From top to bottom in the figure, the mean particle diameter is 1 μm, 10 μm, and 100 μm. The particle diameters are log-normal distributed with standard deviations that are 10% of the mean diameter. The reflectance spectra from polydispersed particle distributions are more useful for gaining insight into real-world situations because there are many resonant features in perfectly spherical particles that are typically not present in irregularly-shaped particles. These features can often be eliminated by averaging over a range of particle sizes.

The simulated spectra appear to be quite complicated considering the fact that they are produced by materials with a single absorption feature. However, they can be mostly understood in a qualitative sense by appealing to some well-known properties of scattering by small particles. First of all, small particles scatter light nearly isotropically, whereas large particles have a very large and narrow forward scattering lobe. The scattering lobe becomes narrower as the particle size increases or as the real part of the refractive index approaches unity. This explains the fact that in the top row, which represents particles much smaller than the wavelength, the reflectance spectra are nearly identical in the forward and backward directions. In the middle row, where the particle sizes are on the order of the wavelength, the magnitude of the reflectance in the forward direction is much greater than the magnitude of the reflectance in the backward direction. In the bottom row, where the particle sizes are much larger than the wavelength, the magnitude of the reflectance in the forward direction is still much larger than in the backward direction, but the difference in magnitude is not as great; this is because the forward scattering lobe is so narrow that the 10° offset from the propagation direction falls mostly outside of the lobe.

The shape of the reflectance spectra as a function of the wavenumber can be qualitatively understood as follows. Relative to the spectrum shown in gray which represents reflectance from a particle with no

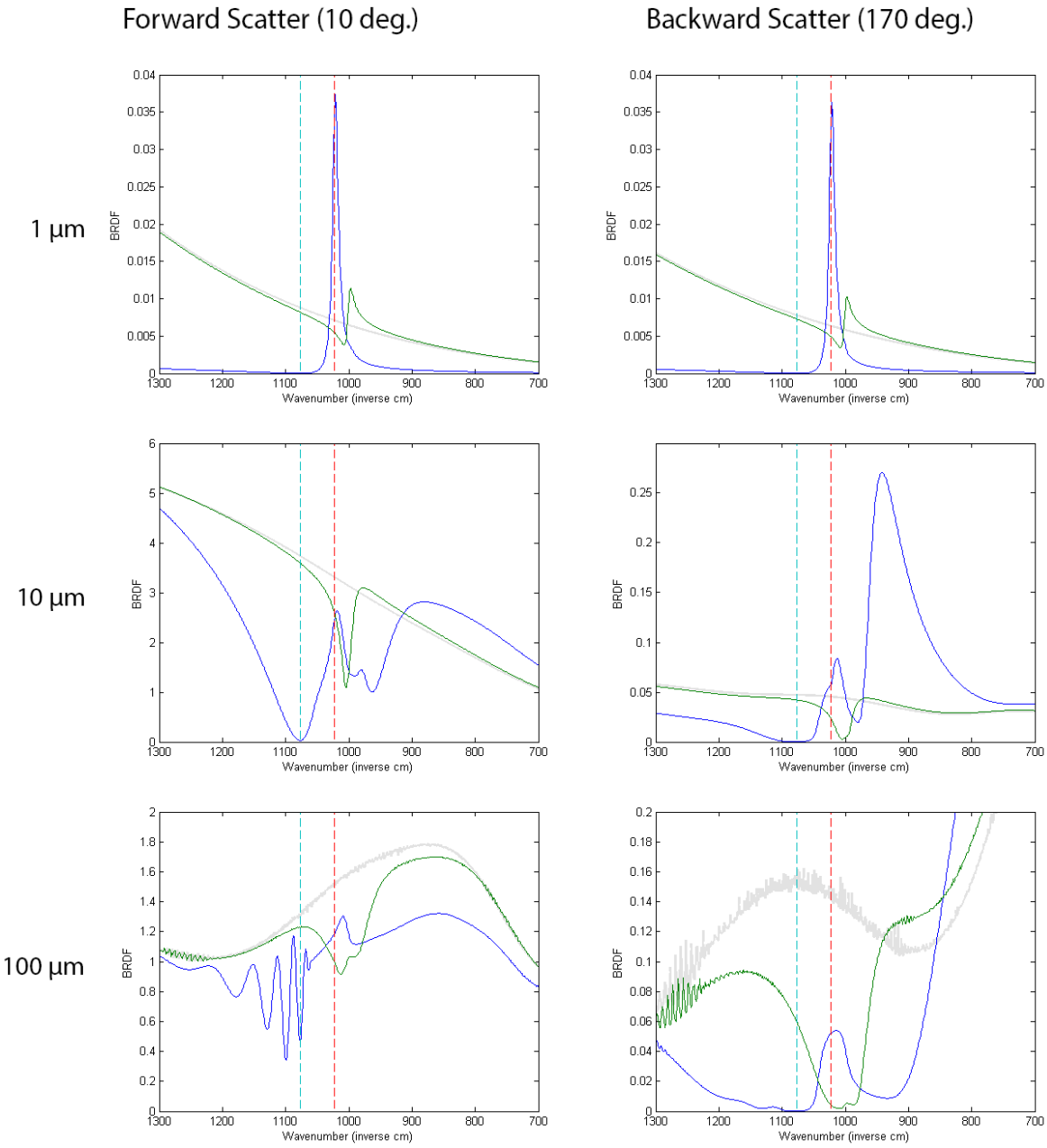

Figure 2.3: Simulations of reflectance spectra of isolated particles. The left half of the figure represents scattering at an angle of 10° from the incident direction, and the right half of the figure represents scattering at an angle of 170° from the incident direction. The top row represents a particle distribution with a mean diameter of 1 μm; the middle row has a mean diameter of 10 μm; and the bottom row has a mean diameter of 100 μm. The standard deviations of the particle sizes are 10% of the means. The blue curve is a highly absorbing material (Material 1), and the green curve is a weakly absorbing material (Material 2). The light gray curve represents a material with a constant refractive index of 1.5. The Frohlich frequency is shown in red, and the Christiansen frequency is shown in cyan.

absorption feature, there is an absorption valley in which the reflectance decreases as the wavenumber approaches the absorption peak. However, as the wavenumber approaches the absorption peak, the refractive index contrast between the particle and air increases, which has the effect of creating a reflectance peak at the bottom of the valley. The qualitative differences in the shape of the spectra with changes in particle size or absorption strength can be understood to a large extent by examining the relative contribution of the absorption valley and the reflectance peak. In addition, there are two frequencies of light that are important in determining the shape of the spectra for strongly absorbing materials. The Frohlich frequency (shown in the figures with a dashed magenta line) is the frequency at which the real part of the permittivity is -2; at this frequency, there is a very strong resonance which causes a peak in the scattering efficiency for small particles. The Christiansen frequency (shown in the figures with a dashed cyan line) is the frequency at which the complex refractive index is closest to 1; at this frequency, the reflectance is nearly zero because the refractive index contrast between the particle and air is very small. For weakly absorbing materials such as Material 2, neither of these frequencies have any meaning because there is no frequency at which the complex permittivity approaches -2 or 1.

In the Rayleigh limit, the scattering efficiency is given by the following equation:

$$Q_S = \frac{8}{3}\pi^4 \left(\frac{D}{\lambda}\right)^4 \frac{|\epsilon - 1|^2}{(\epsilon' + 2)^2 + \epsilon''^2}. \tag{2.3}$$

In the top row of Figure 2.3, the particles are significantly smaller than the wavelength and thus Equation 2.3 applies. The reflectance peak dominates over the absorption valley for both strongly absorbing particles and weakly absorbing particles, but for different reasons. In strongly absorbing particles, there is a very large peak at the Frohlich frequency where the complex permittivity approaches -2. In weakly absorbing particles, the imaginary part of the permittivity (and refractive index) is small compared to the real part, so the refractive index contrast between the particle and air dominates. Thus, the shape of the spectrum is very similar to a first-surface reflectance spectrum.

When the particle diameter is on the order of the wavelength, as in the middle row, there is no longer a simple equation that describes the reflectance as a function of permittivity/refractive index. However, the overall shape can still be understood as an absorption valley plus a reflectance peak. The strength of the reflectance peak relative to the absorption valley is much smaller than for the top row; for weakly absorbing particles the reflectance peak is barely visible and the reflectance spectrum resembles a transmittance spectrum. The depth of the absorption valley relative to the baseline is greater in the backward scattered spectrum than in the forward scattered spectrum because, to a first approximation, the light that contributes to the forward scattered spectrum traverses the particle once,

whereas the light that contributes to the backward scattered spectrum traverses the particle twice. For the strongly absorbing particle, the peak has shifted slightly away from the Frohlich frequency and towards the resonant frequency of the oscillator. Finally, an important feature to note is that in the forward scattered spectrum, there is a sharp dip around the Christiansen frequency, whereas the backward scattered spectrum is very flat around the Christiansen frequency. There are two reasons for this. The first is that, as mentioned above, the absorption valley in the backscattered spectrum is deeper than in the forward spectrum. The second reason has to do with the mechanism by which the forward and backward scattered spectra are created. The forward-scattered spectrum is created by light being diverted slightly away from its direction of propagation; thus, even a small refractive index contrast between the particle and the air results in significant scattering, and so the reflectance returns to the baseline much more quickly after dipping at the Christiansen frequency. On the other hand, the backward scattered spectrum is more similar to a single-surface reflectance, and thus remains low except for high refractive index contrasts.

Finally, consider the case where the particle diameter is much larger than the wavelength (bottom row). Once again, the absorption valley is much larger for the backward scattering than for the forward scattering. For the weakly absorbing particle, the reflectance spectrum again resembles a transmittance spectrum, although the reflectance peak at the bottom of the absorption valley is slightly more prominent. The reflectance peak in the strongly absorbing particle has moved farther away from the Frohlich frequency. The minimum at the Christiansen frequency for the strongly absorbing particle is much sharper than in the middle row; the interference pattern that appears around the Christiansen frequency is due to interference between light that travels through the particle and light that travels around the particle. The spacing between peaks in the interference pattern is approximately

$$\Delta\widetilde{\nu} = \frac{1}{Dn}, \tag{2.4}$$

where $\Delta\widetilde{\nu}$ is the spacing between peaks in wavenumbers, D is the diameter of the particle, and n is the real part of the refractive index. In theory, this equation could be used in reverse to get an estimate of the size of the particles in the sample. If $\widetilde{\nu}_{peak}$ is the wavenumber at the first peak at a lower wavenumber than the Christiansen frequency, and $n(\widetilde{\nu}_{peak})$ is the real part of the refractive index at that wavenumber, then the size of the particles in the sample is approximately

$$D = \frac{1}{2\widetilde{\nu}_{peak}(1 - n(\widetilde{\nu}_{peak}))}. \tag{2.5}$$

The final thing to note about the bottom figure is that, for the strongly absorbing particle, the

reflectance spectrum is almost identical to the single-surface reflectance spectrum. In fact, as one might expect, the single-surface reflectance exactly describes the reflectance spectrum as the particle size goes to infinity. This is of course also true for the weakly absorbing particles; however, the particle must be very large in order for the baseline reflectance to drop below the reflectance peak. Thus, for the range of sizes that are represented in the figure, the single-surface reflectance is a good approximation to the reflectance spectrum for small, weakly absorbing particles or large, strongly absorbing particles.

2.4 Nonspherical Particles

The results of the previous section were based on the assumption that the particles in the sample are spherical. However, there are several important differences in the reflectance spectra of irregularly shaped particles and spherical particles. Hapke, in *Theory of Reflectance and Emittance Spectroscopy* [4], notes some of these differences:

> ...If a particle is translucent, that is, if it has few internal scatterers and is not completely opaque, its phase function is dominated by a strong, broad, forward scattering lobe caused by refracted, singly transmitted rays.... This lobe is weaker for irregular particles than for spherical ones, but it occurs for particles of any shape or degree of surface roughness. Its amplitude decreases as the absorption coefficient increases. (page 115)
>
> ...In an irregular particle the intensity at intermediate angles is increased markedly, by as much as an order of magnitude, over that for a sphere. (page 115)
>
> ...In scattering by an irregular particle, some of the energy that would have gone into the strong, forward-refracted and weaker, backward-internally-reflected peaks if the particle were a sphere is redirected and internally scattered into the sideways directions. (page 117)
>
> ...Highly absorbing particles with large imaginary refractive indices and smooth surfaces have phase functions that are slightly forward-scattering.... However, if their surfaces are rough the phase function can be approximately isotropic or even backscattering. (page 118)
>
> ...The phase functions of large irregular particles tend to be much more isotropic than perfect spheres and may even be backscattering. There are two reasons for this. First, as the particle size increases, surface irregularities become large enough to cast shadows, which are more visible at larger phase angles.... Second, large real particles tend to be composite and made up of many smaller particles that can act as internal scatterers and may also be absorbing. (page 118)

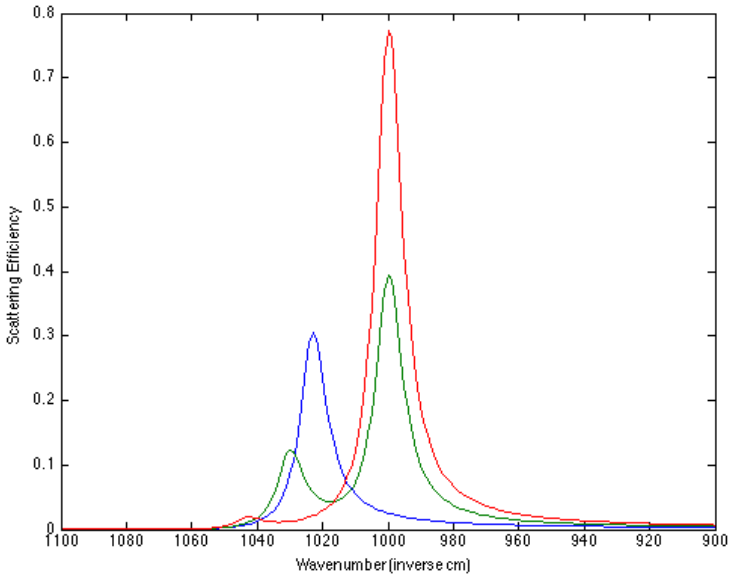

Figure 2.4: The scattering efficiency from 1 μm particles of various shapes. The blue curve is a sphere; the green curve is a needle; and the red curve is a disk.

In short, irregular particles tend to scatter more isotropically than spherical particles and have forward scattering lobes that are not as narrow. This means that the forward and backward scattered spectra for irregular particles are more similar in magnitude and shape than for spherical particles.

For very small particles, irregularities do not contribute much to the shape of the reflectance spectrum. However, the overall shape of the particle can be a significant factor. Figure 2.4 shows the scattering efficiency of Material 1 for a 1 μm spherical particle (blue), needle-shaped particle (green), and disk-shaped particle (red). The equations used to calculate the scattering efficiencies are given in Reference [8]. For the spherical particle, the peak is located at the Frohlich frequency as expected. However, the needle and disk shaped particles have peaks at the resonance frequency of the Lorentz oscillator (1000 cm^{-1}), as well as smaller peaks at higher frequencies.

2.5 Particles on a Smooth Surface

For a particle on a surface, there are two different paths light can take before scattering off the particle, as shown in Figure 2.5. Path 1 consists of light that is scattered by the particle directly, and Path 2 consists of light that is first reflected off the surface and then scattered by the particle. After the light scatters off the particle, there are also two paths by which the scattered light reaches the observer. The total reflectance from the particle on the surface can be calculated by using Mie Theory combined with Fresnel reflection to calculate the contribution to the reflectance from each path, taking into account

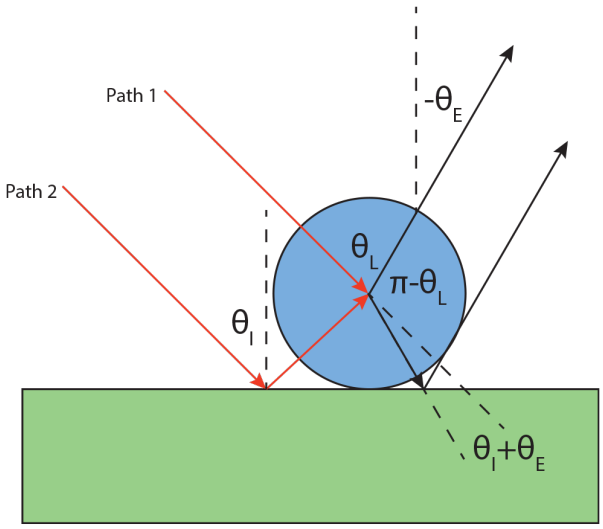

Figure 2.5: The double interaction model. Light interacts with the particle via two different paths. The red arrows represent the collimated incident light, and the black arrows represent the scattered light.

shadowing factors. This model of reflectance is known as the double-interaction model. NIST has an online C++ library called SCATMECH which has a class that implements the double-interaction model. It also has a class that implements the exact solution to the scattering of light by a spherical particle on a surface, as put forth by Bobbert and Vlieger [10]; as might be expected, the exact solution is much more computationally intensive than the double-interaction model. Appendix A.2 shows C++ code that implements the Bobbert-Vlieger model and the double-interaction model from the SCATMECH library.

In general, path 1 is often sufficient to approximate the reflectance spectrum. Thus, we can make a very simple model in which the reflectance spectrum is simply the sum of the backscattered light and the scattered-reflected light:

$$r = Mie(\pi - \theta_L) + |r_{air,surface}(\theta_E)|^2 Mie(\theta_E + \theta_I), \tag{2.6}$$

where $Mie(0)$ is the BRDF predicted by Mie Theory in the exact forward direction and $r_{air,surface}(\theta_S)$ is the Fresnel coefficient for the air-surface interface at an angle of incidence of θ_S. In the equation above, it is assumed that the incident direction, normal vector, and emittance direction are all in the same plane. This simple model is useful as a way to more easily understand the phenomenology of the reflectance spectra. In any real calculation, it is usually best to use the double interaction model because it is just as fast but typically more accurate. The exact Bobbert-Vlieger model, of course, is much more computationally intensive. Figure 2.6 shows calculations of the BRDF of a sodium chlorate particle on a

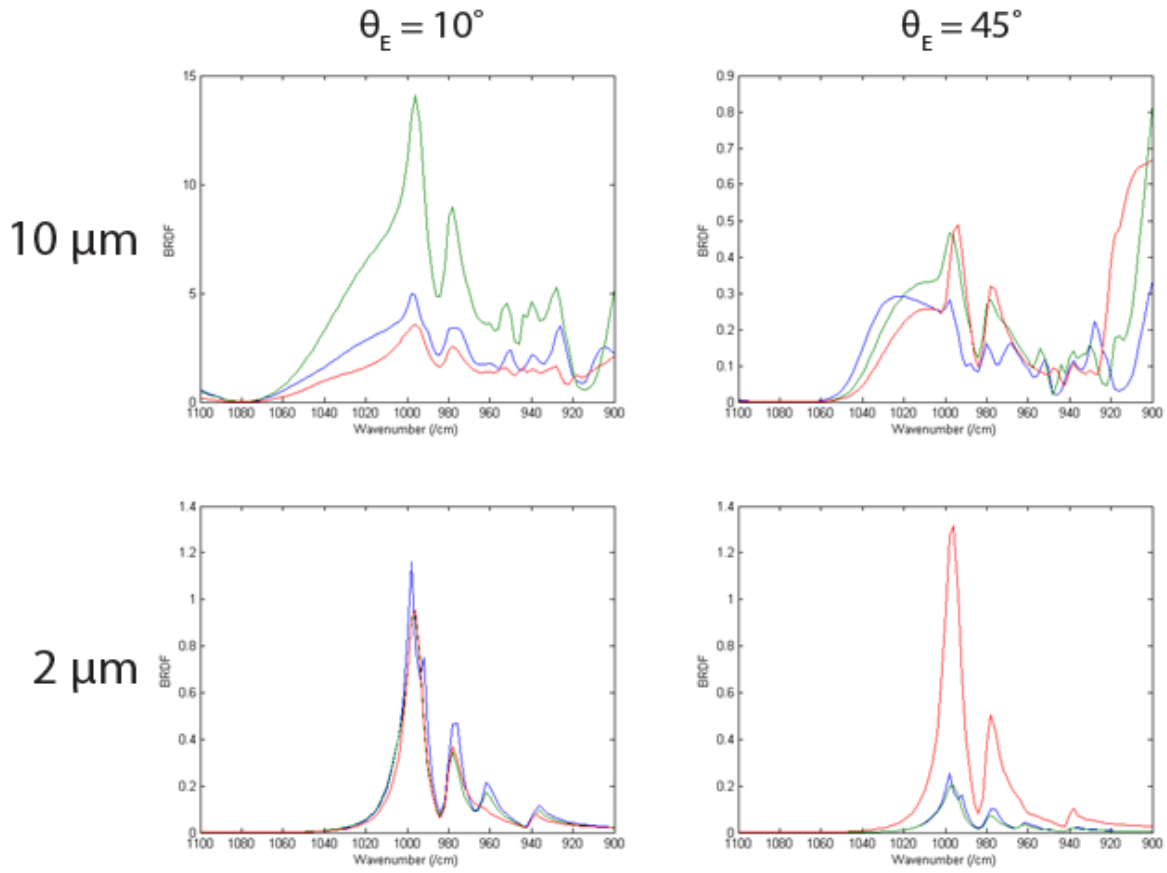

Figure 2.6: A comparison of three different models for a sodium chlorate particle on a surface. The exact Bobbert-Vlieger solution for a spherical particle on a surface (blue), the double interaction model (green), and the simplified interaction model given in Equation 2.6 (red). The refractive index of the surface was assumed to be $10 + 100i$. In all cases, it was assumed that $\theta_L = 0$.

gold surface using the exact Bobbert-Vlieger solution (blue), the simplified interaction model according to Equation 2.6 (green), and the double interaction model (red). The top half of the figure represents a particle with a diameter of $10\,\mu$m, and the bottom half of the figure represents a particle with a diameter of $2\,\mu$m. The left half of the figure represents a sample angle of 10°, and the right half represents a sample angle of 45°. The laser angle is assumed to be zero. The simplified interaction model provides a fairly good approximation of both the shape and magnitude of the reflectance spectra. The refractive index of sodium chlorate that was used in these calculations were taken from Reference [9]; the real and imaginary parts as a function of wavenumber are shown in Figure 2.7.

Given the fact that the reflectance spectrum of a particle on a surface can be modeled reasonably well by the simple Equation 2.6, we can draw the following conclusions about how the magnitude and shape of the spectra are expected to change with viewing angle and surface reflectivity:

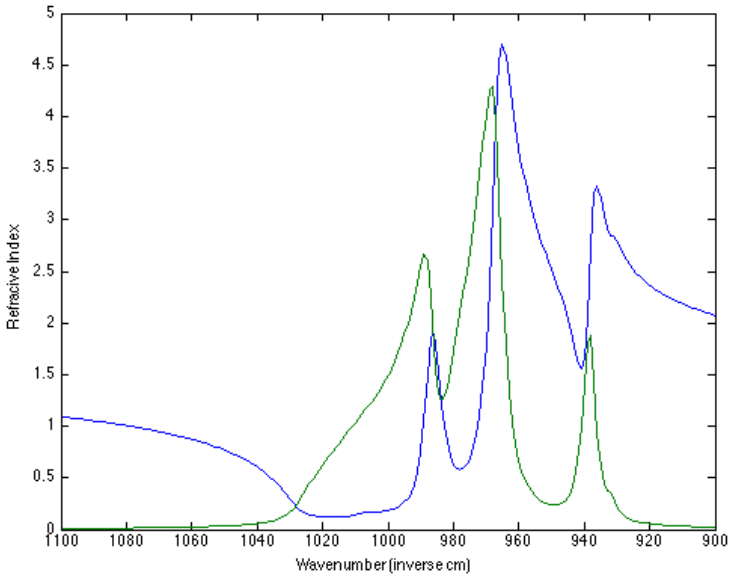

Figure 2.7: The refractive index of sodium chlorate. The real part is shown in blue, and the imaginary part is shown in green.

- Weakly reflective surface: when the surface is weakly reflective, the contribution from the second term in Equation 2.6 is negligible. Thus, the reflectance spectrum should resemble a backscattered reflectance spectrum regardless of the sample angle.
- Strongly reflective surface: when the surface is strongly reflective, the reflectance spectra will resemble a forward-scattered spectrum at small sample angles and laser angles; the contribution from the forward-scattering will decrease as the sample angle or laser angle increases because less of the forward scattered lobe will be reflected back to the camera.

2.6 Experiment: Sodium Chlorate Particles on Gold and Silica

Thus far, all of the conclusions have been based purely on theoretical considerations. But as Richard Feynman once said, "We are not to tell nature what she's gotta be... She's always got a better imagination than we have." In this section, the results of an experiment with sodium chlorate particles on a gold surface are examined and compared with the theoretical predictions.

Experiment Setup

The lasers were pulsed at 10 kHz. The first laser was scanned at wavenumbers $926\,\mathrm{cm}^{-1}$ through $1004\,\mathrm{cm}^{-1}$ in steps of $1\,\mathrm{cm}^{-1}$, with a pulse width of $1.5\,\mu\mathrm{s}$. The second laser was scanned at wavenumbers

$1016\,\mathrm{cm}^{-1}$ through $1100\,\mathrm{cm}^{-1}$ in steps of $1\,\mathrm{cm}^{-1}$, with a pulse width of $0.5\,\mu$s. The first laser was pulsed longer than the second laser because it had less power. The DFPA camera with $f = 50\,\mathrm{mm}$ lens, performed multi-pulse integration and background subtraction as described in Section 1.2. The camera performed a count up for $4\,\mu$s beginning $0.3\,\mu$s before the laser pulse, and then counted down for $4\,\mu$s beginning $6\,\mu$s after the count up. Each camera frame contained 50 count-up/count-down sequences, and 128 frames were taken at each wavelength.

The samples were prepared by crushing sodium chlorate pellets into a powder and then placing a small amount of the powder onto a gold mirror and a silica slide with a metal spatula. Each sample was placed horizontally a distance of 57 cm from the DFPA lens. An aluminum mirror was placed above the sample and allowed to pivot about a horizontal axis. For each sample, the mirror was set to angles of 45°, 50°, 60°, and 70° away from the horizontal plane. These mirror angles correspond to effective sample angles of 0°, 10°, 30°, and 50°. For each of these sample angles, a hyperspectral image cube was obtained of the sample at laser angles of 7° and 35°. At each sample angle and laser angle, a diffuse gold standard was also imaged.

The particle size distribution of the sodium chlorate powder was determined using an Olympus BX61 microscope with a 5x objective. A custom Matlab script was used to count the particles and determine their areas. The areas were converted into diameters of spheres with equivalent cross-section area. It was found that the average particle diameter was $78\,\mu$m, with a standard deviation of $74\,\mu$m.

Results

Figure 2.8 shows an image of the diffuse gold standard at $1000\,\mathrm{cm}^{-1}$. To normalize the laser power, the sum of the counts in the pixels of the illuminated region of each diffuse gold image was set to a constant value, and then the total number of counts in the region of interest of the sample was divided by the total number of counts in the same region in the (normalized) diffuse gold image. Figure 2.9 shows images of the sodium chlorate on a gold mirror (top) and silica slide (bottom) at an effective sample angle of 0° and a laser angle of 7°. The white rectangles show the regions that were used to obtain the reflectance spectra. Outside these regions, reflectance from the laser can still be seen because the sample region was surrounded by paper to aid in alignment of the laser.

The top of Figure 2.10 shows the reflectance spectra for the gold mirror (left) and the silica slide (right) with a laser angle of 7°. The bottom part of the figure shows the spectra calculated using the double-interaction model. The calculations assumed a log-normal distribution of particles with a mean diameter of $78\,\mu$m and a standard deviation of $74\,\mu$m. An effective sample angle of 0° is shown in blue, 10° is shown in green, 30° is shown in red,and 50° is shown in cyan. The spectra have been normalized

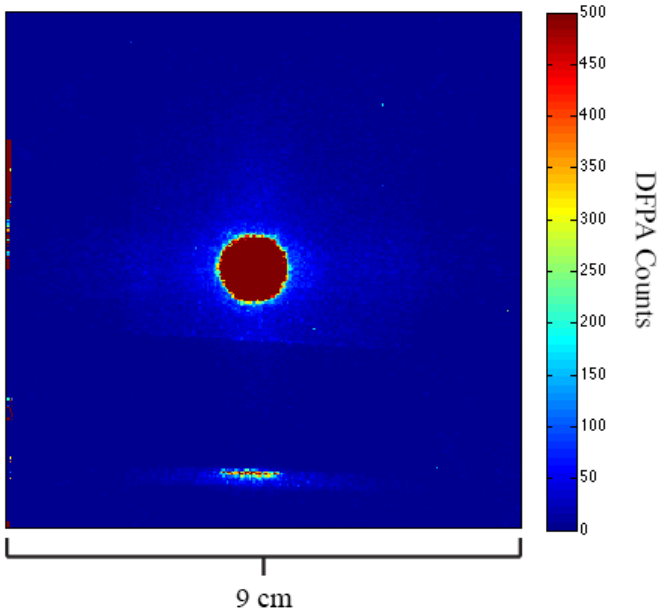

Figure 2.8: Image of gold standard at 1000 cm^{-1}.

so that the maximum value of the reflectance at a sample angle of 0° on the gold mirror is equal to 1.

Figure 2.11 shows the same information as Figure 2.10 for a laser angle of 35°. The magnitude of the spectra are comparable to the spectra in Figure 2.10; that is, a reflectance value of 1 represents the maximum reflectance when the sample angle was 0° and the laser angle was 7° on the gold mirror.

Discussion

As expected, the reflectance decreases much more rapidly with increase in sample angle when the laser angle is small than when the laser angle is large because more of the strong forward lobe is reflected back to the observer at small laser angles and sample angles. That is why the reflectance has to be plotted on a log scale in Figure 2.10. However, the decrease in reflectance is smaller than that predicted by the double interaction model. This is most likely due to the fact discussed above that irregular particles scatter more isotropically than spherical particles. For a similar reason, the difference in magnitude between the small-laser-angle spectra and the large-laser-angle spectra is less pronounced in the experimental data than in the theoretical calculations. On the other hand, the theoretical model does a fairly good job at predicting the decrease in the reflectance caused by the more weakly-reflecting silica surface, at least for small-laser-angle case.

One of the most obvious effects of increasing the sample angle is that the dip around the Christiansen frequency becomes less narrow, so that at larger sample angles the reflectance stays at nearly zero around

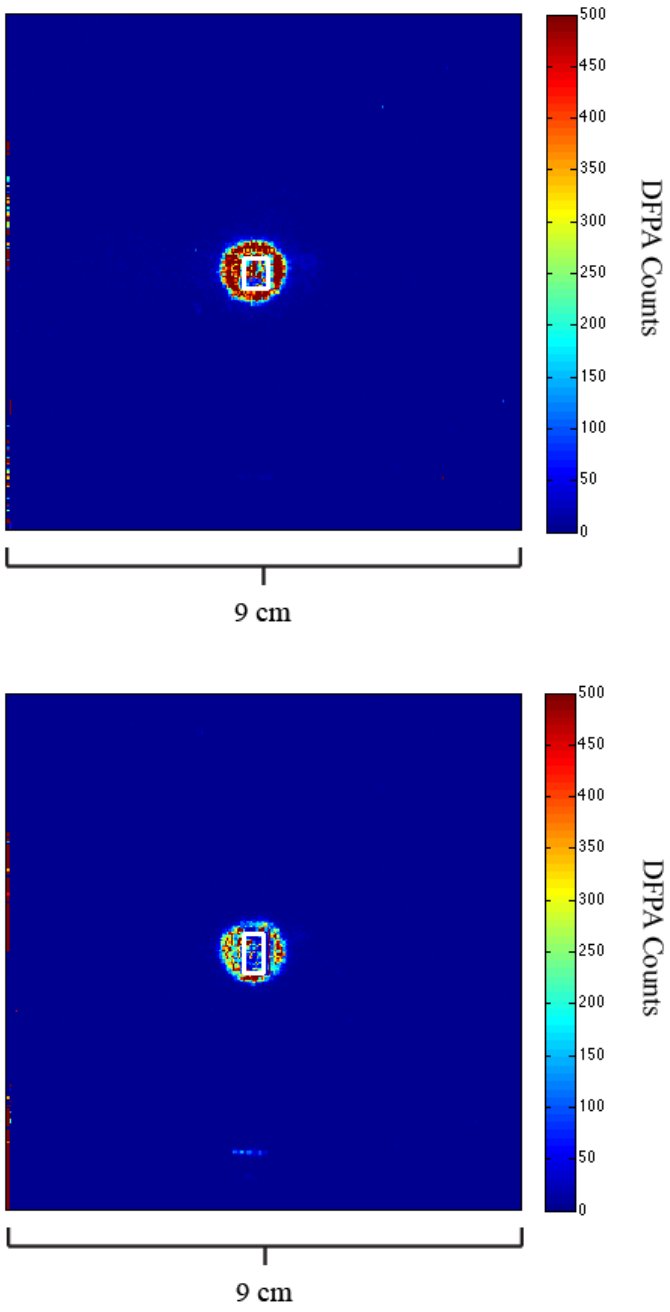

Figure 2.9: Images of sodium chlorate on a gold mirror (top) and silica slide (bottom) at $1000\,\mathrm{cm}^{-1}$. The white rectangles show the regions that were used to obtain the reflectance spectra.

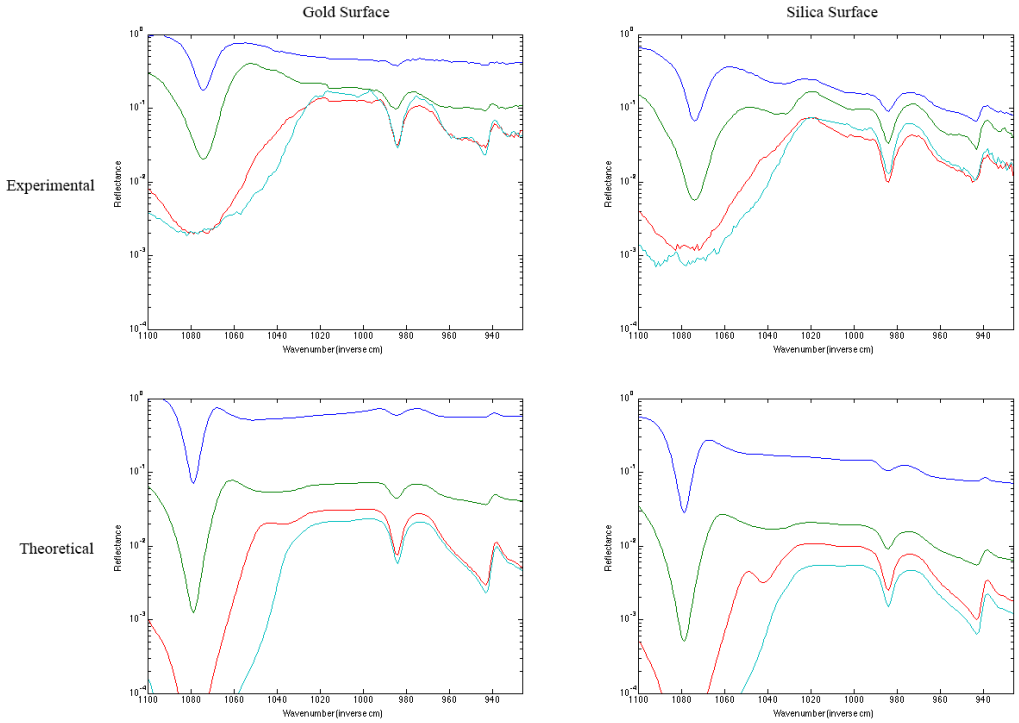

Figure 2.10: Experimental results (top) and theoretical calculations (bottom) for the reflectance spectra of sodium chlorate on a gold mirror (left) and silica slide (right). The laser angle was 7°, and the sample angles were 0° (blue), 10° (green), 30° (red), and 50° (cyan).

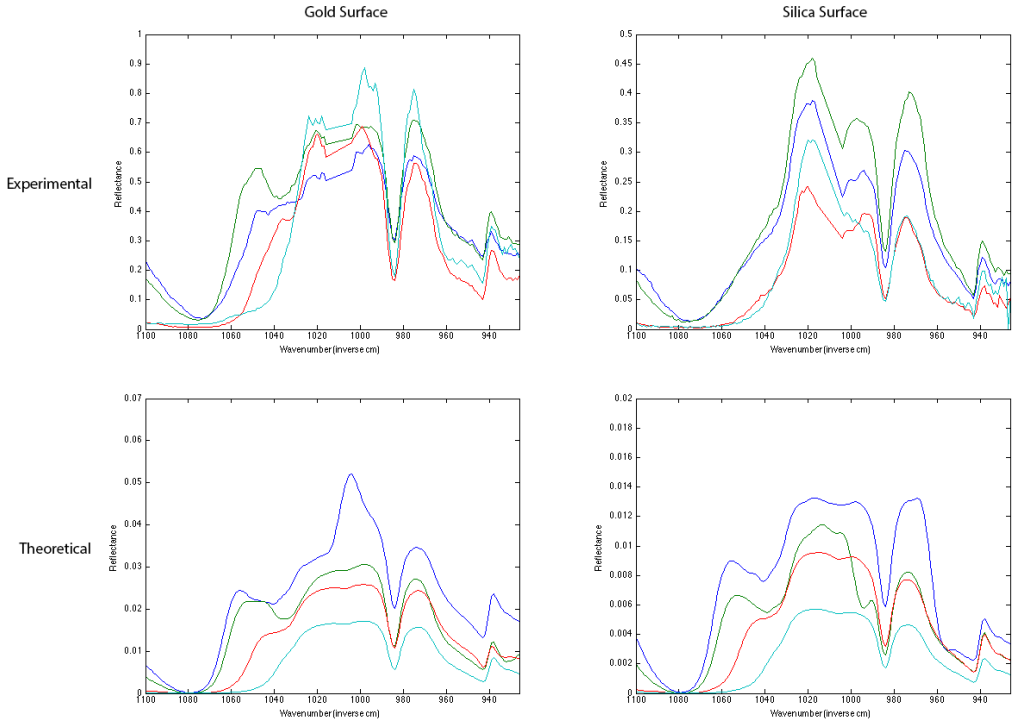

Figure 2.11: Experimental results (top) and theoretical calculations (bottom) for the reflectance spectra of sodium chlorate on a gold mirror (left) and silica slide (right). The laser angle was 35° and the sample angles were 0° (blue), 10° (green), 30° (red), and 50° (cyan).

the Christiansen frequency, relative to the reflectance of the other peaks in the spectrum. This also can be explained by the shift from a predominantly forward-scattered spectrum at small sample angles to a predominantly backward-scattered spectrum at large sample angles. The reason for the increased sharpness of the dip in the forward-scattered spectrum as compared to the backward-scattered spectrum was explained in Section 2.3.

The dips at the Christiansen frequency are not nearly as strong in the experimental spectra as they are in the theoretical spectra. The most likely reason for this is, again, the fact that the particles are irregular. Having many different facets means that there are more opportunities for the light to be reflected, even if the refractive index is very close to 1 at the Christiansen frequency. Also, the location of the Christiansen frequency dip is at a different wavenumber in the experimental data than in the theoretical calculation. The most reasonable explanation for this is that the refractive index values used in the calculation are not perfectly accurate. The method used by the authors in Reference [9] to obtain the refractive index was to adjust Lorentz oscillator parameters until the experimental first-surface reflectance matched the theoretical reflectance. It is difficult to get precise values for the refractive index using this method when the reflectance is very small, as it is near the Christiansen frequency.

In both the small-laser-angle (7°) spectra and the large-laser-angle (35°) spectra, there is a peak at approximately $1057\,\mathrm{cm}^{-1}$ when the sample angle is small, but the peak goes away when the sample angle is large. This peak is present because of the interference pattern around the Christiansen frequency that arises in the forward-scattered spectrum of large particles. Thus, the peak disappears at high sample angles because the forward-scattered spectrum no longer contributes to the total reflectance spectrum. We can use the spectral location of the peak to estimate the size of the particles in the sample by using Equation 2.5. The real part of the refractive index at $1057\,\mathrm{cm}^{-1}$ is 0.84; therefore,

$$D = \frac{1}{2(1057\,\mathrm{cm}^{-1})(1-0.84)} = 0.0030cm = 30\,\mu\mathrm{m}. \tag{2.7}$$

Thus, the diameter of the particles that is predicted based on the location of the peak is a little less than half of the average diameter that was determined with the microscope. This is not unreasonable because large particles that are very nonspherical would be more appropriately described as a cluster of smaller particles.

2.7 Chapter Summary and Conclusions

The reflectance spectra from particles on a smooth surface can be thought of as a combination of the forward-scattered spectra and the backward-scattered spectra. At small sample angles and laser angles,

the forward-scattered spectra dominates, but its contribution decreases as the sample angle or laser angle increases. Using two simulated materials, the forward and backward scattered spectra of particles of various sizes were examined. One of the main differences between the backward-scattered spectra and the forward-scattered spectra is that the forward-scattered spectra have a much narrower dip at the Christiansen frequency for large, highly absorbing particles. The forward-scattered spectra also have a peak near the Christiansen frequency whose spectral location depends on the size of the particles. Moreover, the reflectance peaks in the forward-scattered spectra are less prominent than in the backward-scattered spectra. All of these results were confirmed by imaging sodium chlorate particles on a gold and silica surface. The double interaction model was able to qualitatively account for the observed spectral features in the experimental data; however, the decrease in the magnitude of the reflectance with increase in sample angle was exaggerated in the theory, which was attributed to the irregularity of the sodium chlorate particles.

The results of this chapter have implications for producing reliable chemical maps. It is clear that the shape of the reflectance spectra can change significantly depending on the particle size and viewing geometry. By understanding how the reflectance spectra is expected to change under different conditions, one can use a priori knowledge of the surface being imaged to improve the detection capability. For instance, if an estimate of the particle size and sample angle can be made, then the reference spectrum used in the detection algorithm can be modified accordingly in order to enhance the detection capability. Conversely, it's possible that the particle size and sample angle can be determined automatically by searching for features in the observed reflectance such as the spectral location of the peak near the Christiansen frequency. Further research is needed in this area.

Chapter 3

Reflectance Spectra of Bulk Powders

3.1 Overview

The previous chapter dealt with particles spaced widely separated on a surface. This chapter is concerned with bulk powders which are thick collections of closely spaced particles. Understanding the reflectance spectra of bulk powders is useful not only for chemical detection of powders but also because it is often the case that the reference spectra that are used in detection algorithms were obtained from bulk powders. Thus, it is important to understand how the reflectance spectra of bulk powders differ from the reflectance spectra of sparse particles. The chapter begins by introducing some common models for the reflectance of collections of particles: the Lommel-Seeliger model and the Hapke Isotropic Multiple Scattering Approximation (IMSA). The Hapke IMSA is applied to the simulated materials from the previous chapter and compare the results to the reflectance spectra of isolated particles. Finally, hyperspectral image cubes of sodium chlorate powder were obtained at many different sample angles and laser angles, and the results are compared to the Hapke IMSA.

3.2 Bulk Powder Reflectance Models

A bulk powder can be modeled as an infinitely deep collection of particles. Each particle can be described by two parameters: the single-scatter albedo w and the scattering profile, $p(g)$. Both of these parameters are functions of wavelength. The single-scatter albedo is defined to be the ratio of the scattering efficiency to the extinction efficiency, where the extinction efficiency is the sum of the scattering efficiency and the absorption efficiency:

$$w = \frac{Q_S}{Q_E}. \tag{3.1}$$

The scattering profile $p(g)$ describes the intensity of the scattered light as a function of g, the angle of the scattered light relative to the incident light. For particles which scatter perfectly isotropically, $p(g) = 1$. Note that, unlike in the case of sparse particles on a surface, the reflectance from a bulk powder does not depend on the actual magnitude of the scattering efficiency of the particle. The reason for this is that any light that is incident on the powder is guaranteed to interact eventually with a particle in the powder since the powder is assumed to be infinitely thick. Thus, the "extinction efficiency" of the entire powder is 1, and therefore to determine the magnitude of the reflectance it is only necessary to compare the fraction of the light that is absorbed by each particle to the fraction of the light that is scattered. This information is contained in the single-scatter albedo.

Both the single-scatter albedo and the scattering profile of a particle can be calculated with Mie Theory. However, since it is often much easier to perform calculations with isotropically scattering particles, one common method is to approximate the narrow forward-scattering lobe of Mie Theory as unscattered light. This approximation is especially appropriate for closely-packed particles because the forward scatter lobe is mainly a result of diffraction, which is suppressed when other particles are nearby. Reference [12] gives an equation for modifying the albedo calculated with Mie Theory to remove the effects of diffraction:

$$w' = \frac{(1 - \xi^2)w}{1 - \xi^2 w}, \tag{3.2}$$

where ξ is the asymmetry parameter calculated by Mie Theory. The asymmetry parameter represents the ratio of forward scattered light to backward-scattered light; an asymmetry parameter of -1 is perfectly backscattering, 0 is perfectly isotropic, and 1 is perfectly forward-scattering.

The Lommel-Seeliger Equation

If we assume that the light which we observe as the reflected light from a bulk powder is comprised solely of light which has been scattered by a single particle within the powder, we are led to the following equation, known as the Lommel-Seeliger equation:

$$r = \frac{w}{4\pi} \frac{\cos(\theta_I)}{\cos(\theta_I) + cos(\theta_S)} p(\theta_L), \tag{3.3}$$

The Lommel-Seeliger equation can be derived as follows: consider a small section $\mathrm{d}z$ of a sample located at a distance z below the surface. The material has a scattering coefficient S and an extinction coefficient E, given in units of inverse distance. If we assume an incident intensity of 1, then the intensity of the light that reaches $\mathrm{d}z$ is $\exp\left(-\frac{Ez}{\cos(\theta_I)}\right)$. Each particle within $\mathrm{d}z$ that is in the line of sight of the emitted direction will scatter this light into the solid angle of the emitted direction by an amount $\frac{S}{4\pi}p(\theta_L)$; thus, the intensity of the light scattered by all of these particles in $\mathrm{d}z$ is $\frac{S}{4\pi}\frac{p(\theta_L)}{cos(\theta_S)}\exp\left(-\frac{Ez}{\cos(\theta_I)}\right)$. This light will be attenuated by an amount $\exp\left(-\frac{Ez}{\cos(\theta_S)}\right)$ before it reaches the surface. Now integrate this expression over all z from 0 to infinity:

$$\begin{aligned}
&\int_0^\infty \frac{S}{4\pi}\frac{p(\theta_L)}{\cos(\theta_S)}\exp\left(-\frac{Ez}{\cos(\theta_I)}-\frac{Ez}{\cos(\theta_S)}\right)\mathrm{d}z \\
&= \frac{S}{4\pi E}\frac{\cos(\theta_I)}{\cos(\theta_I)+\cos(\theta_S)}p(\theta_L) \\
&= \frac{w}{4\pi}\frac{\cos(\theta_I)}{\cos(\theta_I)+\cos(\theta_S)}p(\theta_L).
\end{aligned} \tag{3.4}$$

The Lommel-Seeliger equation is most applicable to low-albedo materials (highly absorbing materials) since it only takes into account singly scattered light. It doesn't consider light that reaches the particle through multiple scattering events.

The Radiative Transfer Equation

In order to take multiple scattering into account, we need to solve the radiative transfer equation. Here is what Hapke says about the assumptions of the radiative transfer equation [4]:

> The fundamental assumption of this formalism is that the medium can be treated as if it were a continuous fluid, each incremental portion of which interacts with other portions independently and incoherently through the processes of absorption, scattering, and emission. The photons are treated as if they were particles diffusing through the medium in a manner similar to gas diffusing through a complicated structure or neutrons diffusing through a nuclear reactor. The theory is not applicable to a medium consisting of particles that are uniformly spaced and regular in shape. However, Mischenko (2002) has shown that for media of widely spaced discrete particles the radiative transfer equation can be derived from statistical electromagnetic theory.

Thus, the equation solves the problem exactly of the reflectance from an infinite collection of particles under the assumption that you can precisely describe the albedo and scattering profile of particles in the

medium, and that each particle is essentially in the far field of other particles.

The radiative transfer equation for a horizontally stratified semi-infinite medium is as follows:

$$-cos\theta \frac{\partial I(\tau,\Omega)}{\partial \tau} = -I(\tau,\Omega) + \frac{w(\tau)}{4\pi}\int I(\tau,\Omega')p(\tau,g')d\Omega' + J\frac{w(\tau)}{4\pi}p(\tau,g)e^{-\frac{\tau}{\mu_0}} + F_T(\tau,\Omega), \tag{3.5}$$

where θ is the angle of emittance at a given point in the material; I is the power emitted into solid angle Ω; τ is the optical depth of the point; $w(\tau)$ is the single scatter albedo; $p(\tau, g)$ is the phase function (single scattering profile); J is the intensity of the incident radiation; $\mu_0 = \cos(\theta_I)$; and $F_T(\tau,\Omega)$ is the thermal radiation. This is a very hard equation to solve under general conditions.

Isotropic Multiple Scattering Approximation

When the scatterers are isotropic (that is, $p(\tau, g) = 1$) and independent of τ, the radiative transfer equation can be solved exactly. The end result is

$$r = \frac{w}{4\pi}\frac{\mu_0}{\cos(\theta_I)+\cos(\theta_S)} H\left[w,\cos(\theta_I)\right] H\left[w,\cos(\theta_S)\right], \tag{3.6}$$

where $H(w, x)$ is the Chandrasekhar H-function, given by the solution to the equation

$$H(x) = 1 + \frac{w}{2}H(x)\int_0^1 \frac{H(x')}{x+x'}dx'. \tag{3.7}$$

Hapke gives the following simple approximation for H(x):

$$H(w,x) = \frac{1+2x}{1+2\gamma x}, \qquad \gamma = \sqrt{1-w}. \tag{3.8}$$

In a later paper, Hapke presents a more accurate approximation for H(x):

$$H(w,x) = \left[1 - wx\left(r_0 + \frac{1-2r_0x}{2}\ln\frac{1+x}{x}\right)\right]^{-1}. \tag{3.9}$$

Equation 3.6 is exact under the assumption of isotropic scattering. In order to approximate nonisotropic scattering cases, Equation 3.6 can be compared with the Lommel-Seeliger equation and reverse engineered in order to write it in a form where we have the sum of the contribution from single scattering (given by Lommel-Seeliger) and the contribution from multiple scattering:

$$r = \frac{w}{4\pi}\frac{\cos(\theta_I)}{\cos(\theta_I)+\cos(\theta_S)}\left[p(\theta_L) + M(w,\theta_I,\theta_S)\right], \tag{3.10}$$

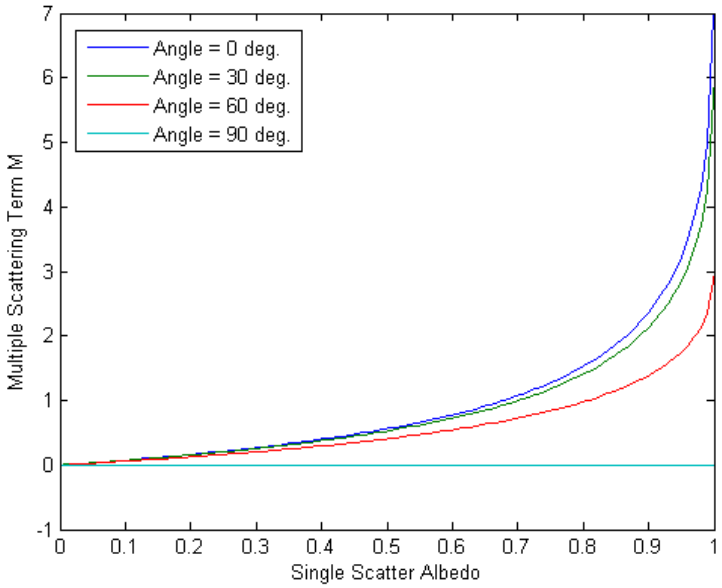

Figure 3.1: The multiple scattering term as a function of single-scatter albedo when the laser angle is zero relative to the viewing direction. The different colors represent different sample angles.

$$M(w, \theta_I, \theta_S) = H\left[w, \cos(\theta_I)\right] H\left[w, \cos(\theta_S)\right] - 1. \tag{3.11}$$

This equation reduces to the exact solution when $p(g) = 1$, and becomes less accurate as the anisotropy of the scattering increases. Hapke dubbed this model the Isotropic Multiple Scattering Approximation (IMSA).

Figure 3.1 shows how the multiple scattering term depends on the albedo for different values of the sample angle. It is assumed that the laser angle is zero. The multiple scattering term is greatest at high albedo and small sample angles. It depends less and less on the albedo as the sample angle increases.

3.3 Calculations With Simulated Materials

Figure 3.2 shows the BRDF of the two simulated materials introduced in Chapter 2, calculated using the Hapke IMSA. The Matlab code used to perform these calculations is shown in Appendixes A.3 and A.4. The single-scatter albedo was calculated using Mie Theory. This method is similar to that described in Reference [22]. It was assumed that the particles scatter isotropically and Equation 3.2 was used to modify the calculated albedo. As before, the top row represents a particle distribution with a mean diameter of 2 μm; the middle row represents a mean diameter of 10 μm; and the bottom row represents a mean diameter of 100 μm. The standard deviations in the particle size distributions are 10% of the means. The left side represents a sample angle of 0°, and the right side represents a sample angle of

89°. The laser angle is zero. Once again, the Frohlich frequency is shown in red, and the Christiansen frequency is shown in cyan. Material 1 (the strongly absorbing material) is shown in blue and Material 2 (the weakly absorbing material) is shown in green.

As expected, the reflectance at a large sample angle is significantly less than the reflectance at a small sample angle. Unlike with scattering from single particles, the reflectance peak for the strongly absorbing material remains at the Frohlich frequency for large particles. There is still the general shape of the absorption valley and reflectance peak, but the spectra are much simpler than the spectra for single particles. As before, the weakly absorbing particles has a transmittance-like spectrum, whereas the strongly absorbing particles have a more reflectance-like spectrum. The absorption valleys are much narrower at the high sample angle than at the low sample angle. This is due to the fact that at higher sample angles there is less of a contribution from multiple scattering (as shown in Figure 3.1), so there are fewer chances for the light to be absorbed.

3.4 Experiment: Sodium Chlorate Bulk Powder

The experiment described in Section 2.6 was repeated with the sodium chlorate powder placed in a square paper container. Figure 3.3 shows an image of the diffuse gold standard at $1000\,\mathrm{cm}^{-1}$, and Figure 3.4 shows an image of the bulk powder sample at $1000\,\mathrm{cm}^{-1}$. The region that was used to obtain the reflectance spectra is indicated. The left part of Figure 3.5 shows the reflectance spectra for a laser angle of 7° and the right part o Figure 3.5 shows the reflectance spectra for a laser angle of 35°. Effective sample angles of 0°, 10°, 30°, and 50° are shown in blue, green, red, and cyan respectively. The bottom part of the figure are the theoretical spectra calculated with the Hapke IMSA, using Mie Theory to calculate the single-scatter albedo. The particle size distribution used in the calculations were the same as for the experiment in Section 2.6: log-normal distribution with a mean diameter of $78\,\mu$m and a standard deviation of $74\,\mu$m. The calculations assumed isotropic scatterers with albedo modified according to Equation 3.2. As with the previous experiment, the experimental design only allows for the relative magnitude of one reflectance spectrum in the experiment to be compared with the magnitude of another reflectance spectrum in the experiment. The absolute value of the BRDF cannot be obtained. Thus, both the experimental spectra and the theoretical spectra were normalized such that the maximum of the spectrum with a 7° laser angle and 0° sample angle is 1.

The theoretical calculations are fairly good at predicting the overall shape of the reflectance spectra, as well as the decrease in reflectance as the sample angle increases. However, there is a very large discrepancy between the magnitude of experimental reflectance spectra for the large-angle case and the

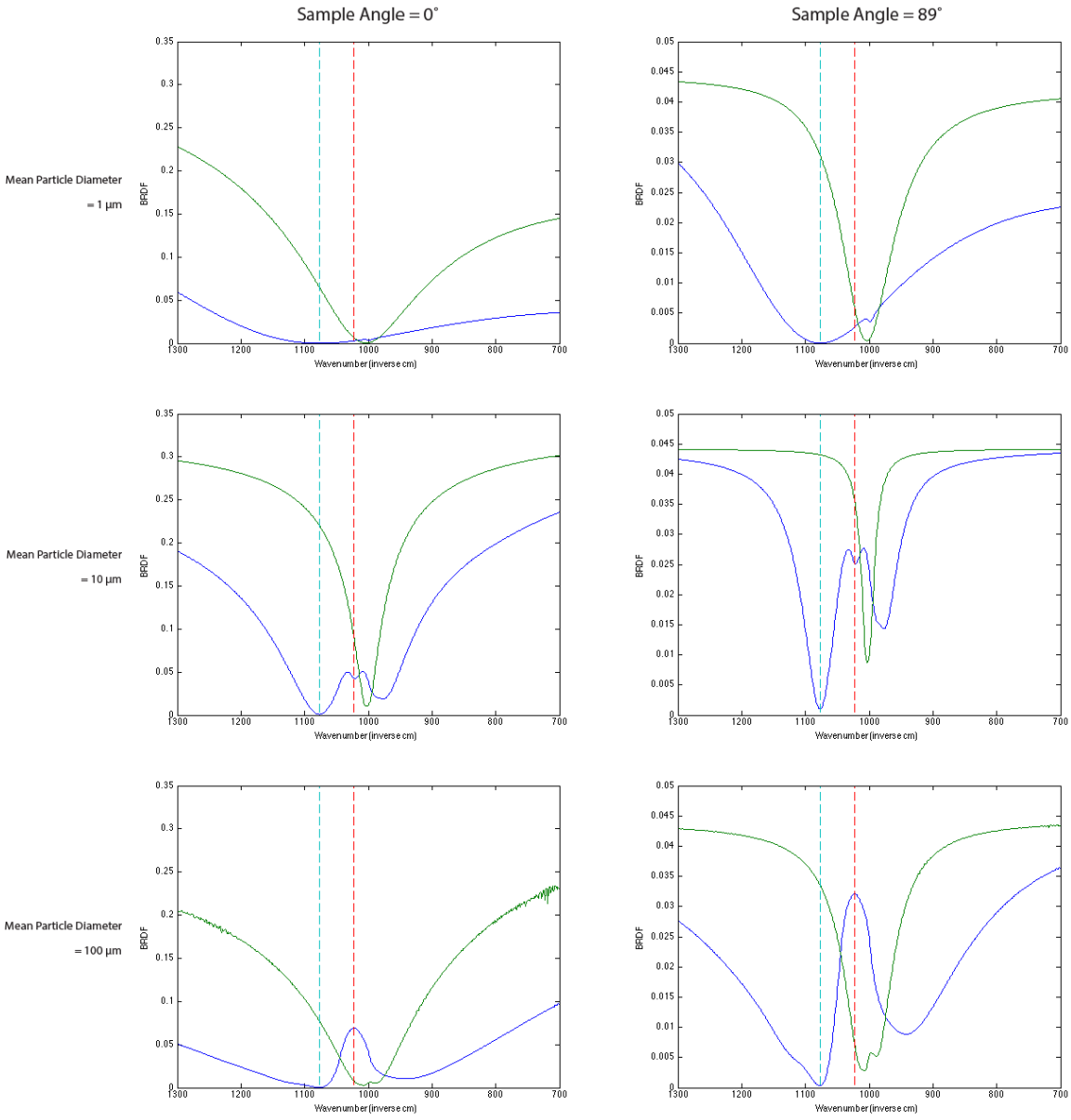

Figure 3.2: Simulations of reflectance spectra from a bulk powder using Mie Theory and the Hapke IMSA. As before, the top, middle, and bottom row represent particle distributions with a mean diameter of 1 μm, 10 μm, and 100 μm respectively. The standard deviations of the particle sizes are 10% of the means. The blue curve is Material 1 (a highly absorbing material) and the green curve is Material 2 (a weakly absorbing material). The laser angle is zero. The Frohlich frequency is shown in red and the Christiansen frequency is shown in cyan.

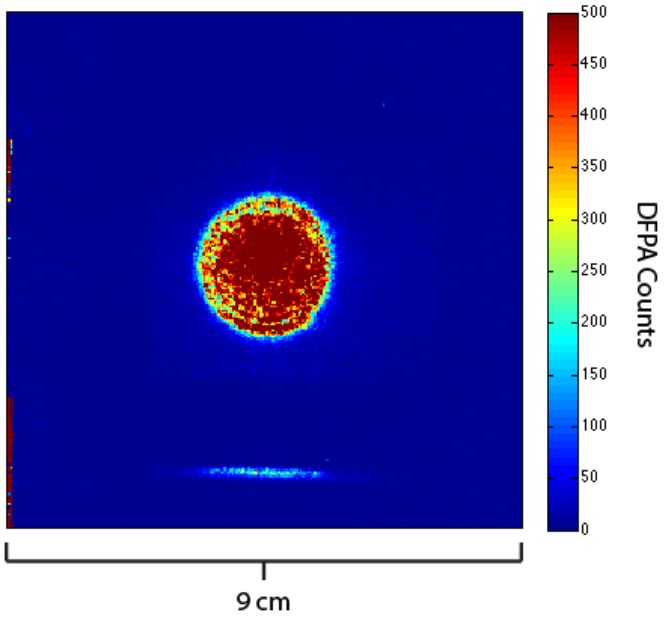

Figure 3.3: Image of gold standard at 1000 inverse cm.

theoretical reflectance spectra. It seems very unlikely, and at odds with the theory, that the reflectance would increase when the laser angle increases. A systematic error in the data collection is most likely the culprit.

3.5 Chapter Summary and Conclusions

The key parameter that determines the reflectance of bulk powders is the single-scatter albedo which is the ratio of the scattering efficiency of a particle to the overall extinction efficiency. Since the single-scatter albedo is a property of the particles as a whole and not dependent on angle, the reflectance spectra from bulk powders are much simpler and less dependent on the viewing geometry than the reflectance spectra of sparse particles. The Hapke IMSA was able to account for the qualitative features of the reflectance spectra of sodium chlorate powder measured at various sample angles and laser angles.

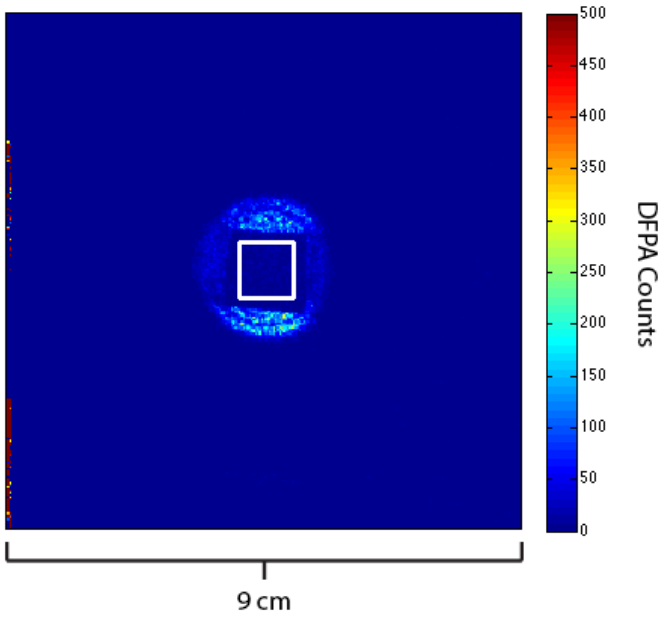

Figure 3.4: Image of sodium chlorate sample at 1000 inverse cm.

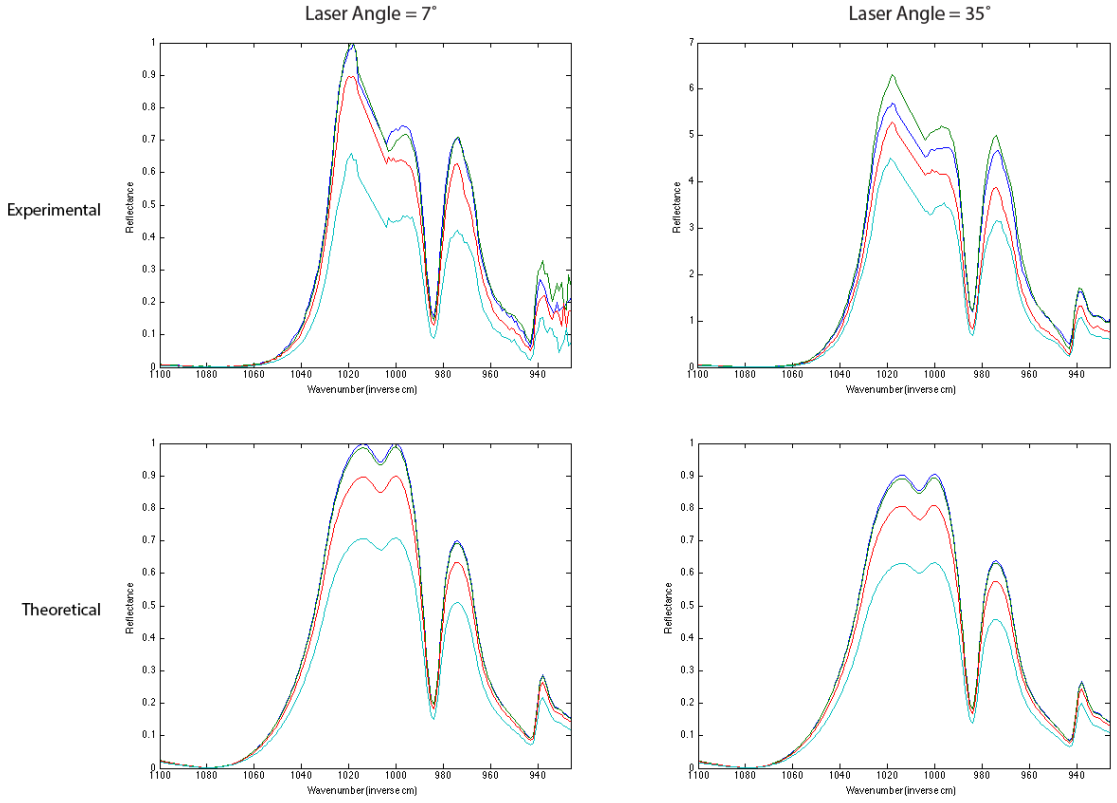

Figure 3.5: The reflectance spectra of sodium chlorate bulk powder. The top and bottom rows are the experimental data and the theoretical calculations, respectively, using Mie Theory and the Hapke IMSA. The left half of the figure represents a laser angle of 7° and the right half of the figure represents a laser angle of 35°. The sample angles are 0° (blue), 10° (green), 30° (red), and 50° (cyan).

Chapter 4

Reflectance Spectra of Thin Films

4.1 Overview

This chapter examines the reflectance spectra of thin films on smooth surfaces, rough surfaces, and porous surfaces. The theory of thin films on a smooth substrate is introduced, and simulations of reflectance spectra using the same simulated materials as in the above chapters are performed. The case of a thin film on a diffusely reflecting surface is examined and the theoretical expectations are tested by taking a hyperspectral image cube of a thin film of diethyl phthalate (DEP) on diffuse gold. Finally, a series of previously collected data from a field-like scenario are examined: DEP on a brick. The reflectance spectra of the DEP on brick as a function of time are studied and it is shown that the spectra can be modeled as a combination of a first-surface reflectance spectrum and a transmittance spectrum. A Monte Carlo method that has potential for enabling a greater understanding of the reflectance from liquids on porous materials is introduced.

4.2 Thin Film on a Smooth Surface

For a thin film on a smooth surface, the light will only be reflected in the specular direction. Consider a film of thickness D with a complex refractive index $N_f = n_f + ik_f$ on a substrate with a complex refractive index $N_s = n_s + ik_s$. If light with wavenumber $\widetilde{\nu}$ is incident on the film at an angle θ from the normal, then the specular reflectance is given by

$$
\begin{aligned}
R &= \left| \frac{r_{air,f} + r_{f,s}\exp(-\alpha D' + i\phi)}{1 + r_{air,f} r_{f,s}\exp(-\alpha D' + i\phi)} \right|^2, \\
D' &= D\cos(\theta), \\
\alpha &= 4\pi k_f \widetilde{\nu}, \\
\phi &= 4\pi n_f \widetilde{\nu} D'.
\end{aligned}
\tag{4.1}
$$

(See Reference [26]). The coefficients $r_{i,j}$ is the Fresnel reflection amplitude between medium i and medium j. For normal incidence,

$$
r_{i,j} = \frac{(n_i - n_j) + i(k_i - k_j)}{(n_i - n_j) + i(k_i - k_j)}. \tag{4.2}
$$

Figure 4.1 shows the normal specular reflectance of the two simulated materials from Chapter 2 for film thicknesses of 0.1 μm (red), 1 μm (green), and an average of thicknesses between 10 μm and 20 μm. The reflectance from large thicknesses are averaged because the reflectance from a single film that is on the order of the wavelength or greater contains many interference structures which distract from the main features. The interference structures are usually not observed in real-life situations because a range of thicknesses are typically present.

The reflectance spectrum from a thin film is a combination of a first-surface reflectance spectrum and a transmittance spectrum. On a very reflective surface (the left half of Figure 4.1), the first-surface reflectance spectrum is only apparent when the absorption feature is strong and the film is thick; otherwise, a transmittance-like spectrum is observed. The minimum of the transmittance-like spectrum gets closer to the absorption maximum as the film thickness decreases. On a weakly reflective surface (the right half of Figure 4.1), the first-surace reflectance dominates when the film is thick, and the peak decreases and shifts to the location of the absorption maximum. A transmittance-like spectrum is not observed on the weakly reflecting surface because almost all of the light that is transmitted through the film is absorbed by the underlying surface. Note that for a material with a strong absorption feature, the reflectance maximum is located at a higher wavenumber than the absorption maxim, whereas for a material with a weak absorption feature the reflectance maximum is located at a lower wavenumber.

The phenomenon whereby a peak is observed on a weakly reflective surface near the wavenumber where a valley is observed on a highly reflective surface has been dubbed "contrast reversal" by some authors (implying that a transmittance-like spectrum is what should "normally" be observed). For instance, in Reference [1], the authors measured the specular reflectance of thin films of TNT of various

thicknesses on an aluminum substrate and on a painted car panel. They found that the spectra from the aluminum substrate closely matched the transmittance spectrum of TNT but the spectra from the painted car panel showed contrast reversal for samples with large thicknesses.

4.3 Thin Film on a Rough Surface

In order to observe the reflectance from a thin film on a smooth surface, the detector must be specularly oriented with respect to the surface. When the detector is not specularly oriented (as is usually the case in standoff hyperspectral imaging), the underlying surface must be diffusely reflective. The reflectance spectrum from a thin film on a perfectly reflecting rough surface is simply the transmittance spectrum, assuming that the film thickness is sufficiently large compared to the roughness of the surface (if this assumption is not made, then the thin film is probably better modeled as a collection of thin films on a smooth surface, in which case the results from the above section apply). Depending on the angle of observation, the magnitude of the reflectance may decrease or increase slightly relative to the underlying surface due to broadening of the scattering profile caused by the presence of the thin film. When viewing the surface along its normal axis, the decrease in observed reflectance due to this effect is approximately given by

$$A = \frac{1}{n^2}, \tag{4.3}$$

where n is the real part of the refractive index of the thin film. This equation arises from a simple application of Snell's Law and the approximation $sin(\theta) \approx \theta$. When the rough surface is not perfectly reflecting, index matching can cause a further decrease in the magnitude of the reflectance, and since the refractive index can be wavelength-dependent, the change in reflectance due to index-matching can also be wavelength-dependent. The total reflectance from a thin film on a rough surface (not taking into account index-matching) is

$$R = AT^2 \exp(-2\alpha D), \tag{4.4}$$

where T is the transmittance at the interface of the thin film and air.

As the thickness of the film decreases, it begins to conform to the countours of the rough surface. When this happens, the shape of the reflectance spectrum approaches the specular reflectance spectra described in the previous section because each individual facet of the rough surface acts like a specular reflector.

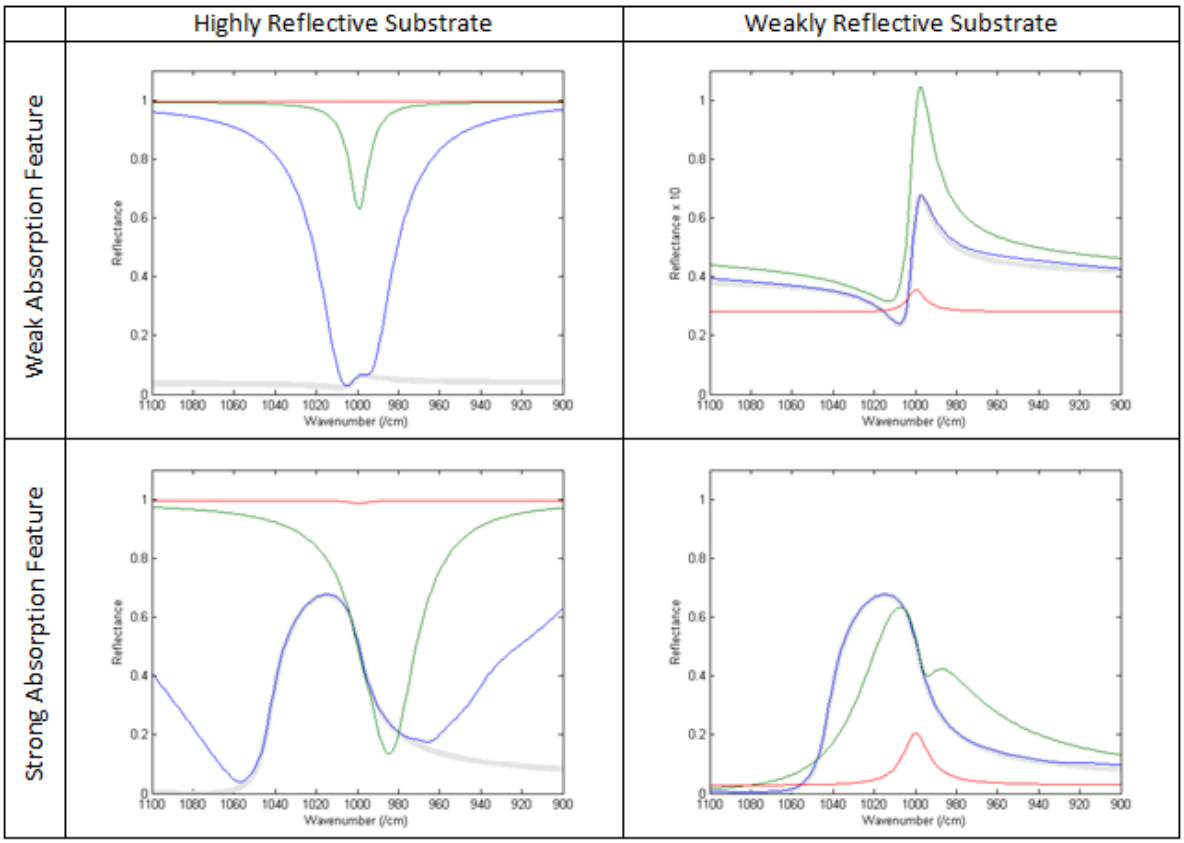

Figure 4.1: Simulations of reflectance from a thin film.

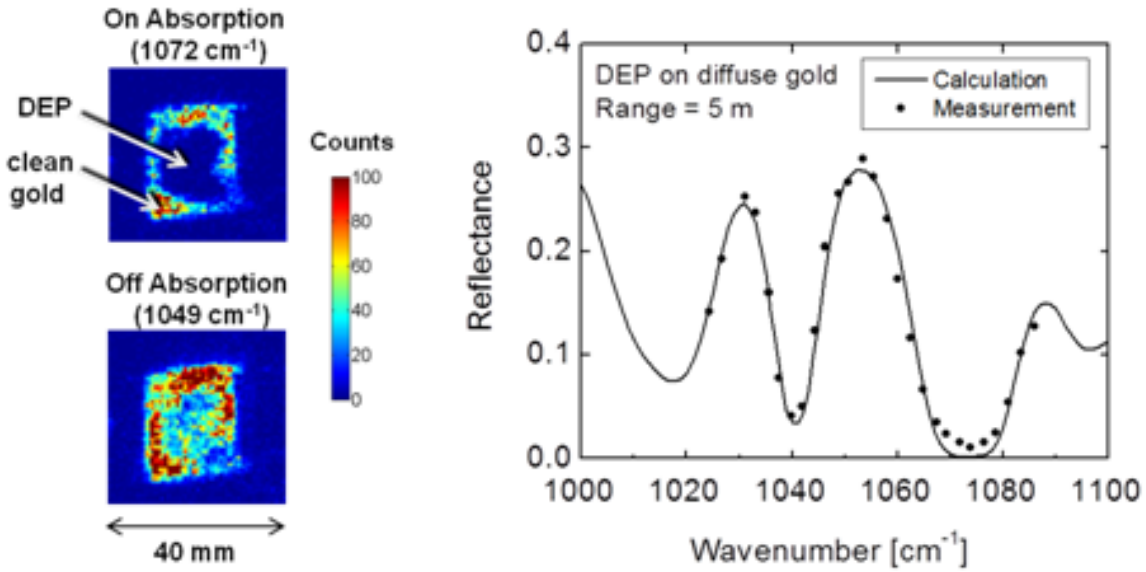

Figure 4.2: The reflectance spectra of DEP on diffuse gold.

Figure 4.2 shows the reflectance spectrum of a thin film of diethyl phthalate (DEP) on a diffuse gold surface. A hyperspectral image cube containing 27 wavelengths was captured using a Wavelength Beam-Combined QCL (WBC-QCL) array (shown as black dots in Figure 4.2). The solid line shows the best least-squares fit to the data calculated using Equation 4.4 allowing A and the thickness D to vary. The fitted value for D was 7.04 μm. The fitted value for A was 0.48, which is close to the value of 0.41 calculated using Equation 4.3. The calculated reflectance spectrum matches the data very well. The small discrepancy can probably be attributed to the fact that the film did not have a perfectly uniform thickness.

4.4 Thin Film on a Porous Surface

As described in Reference [11], 5μL of diethyl phthalate (DEP) was deposited on a concrete brick and hyperspectral images were obtained at times 0, 15, 30, 45, 60, 90, 180, 300, and 360 minutes after deposition. The data was collected by the authors in Reference [11] and the following discussion is my analysis of the data. Figure 4.3 shows the reflectance spectrum of the brick before and immediately after deposition.

The reflectance spectra of the DEP on brick at the various times are shown in green in Figure 4.4. The spectra are normalized to the spectrum of the clean brick. The spectra can be understood as a combination of specular reflectance and diffuse reflectance. The specular portion arises from DEP that

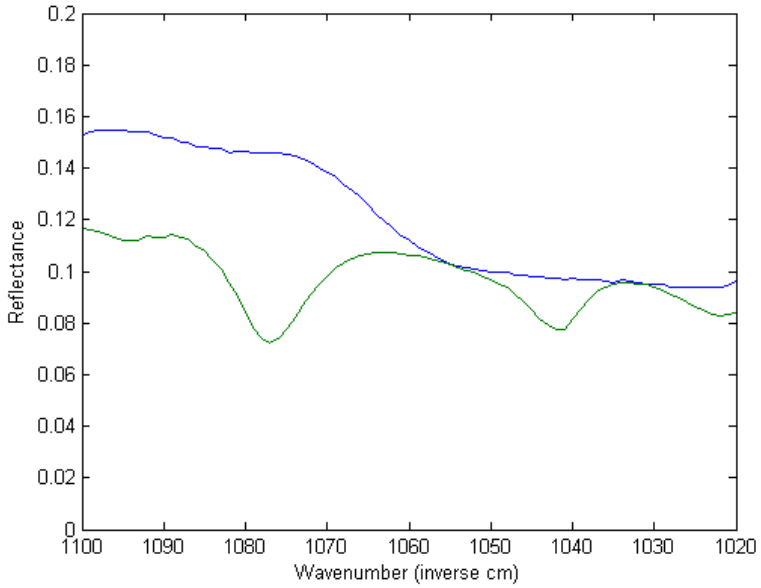

Figure 4.3: The reflectance from clean brick (blue) and DEP on brick (green) immediately after deposition.

conforms to facets on the brick that are specularly oriented with respect to viewing geometry. The specular reflectance as a function of wavenumber can be approximated as the normal-incidence single-surface reflectance of the air-DEP interface:

$$R_{specular}(\widetilde{\nu}) = \left| \frac{1 - N(\widetilde{\nu})}{1 + N(\widetilde{\nu})} \right|^2. \tag{4.5}$$

The diffuse reflectance is the light that is transmitted through the DEP, reflects off the brick, and the is transmitted back through the DEP to the camera. Thus, the diffuse reflectance be approximated by a double-pass transmittance multiplied by the reflectance of the clean brick:

$$R_{diffuse} = R_{clean} \exp(-8\pi k(\widetilde{\nu})\widetilde{\nu} d_{eff}), \tag{4.6}$$

where $k(\widetilde{\nu})$ is the imaginary part of the refractive index and d_{eff} is the effective thickness of the DEP film. Total reflectance is a weighted sum of $R_{specular}$ and $R_{diffuse}$:

$$R(\widetilde{\nu}) = f_s R_{specular} + f_d R_{diffuse}(\widetilde{\nu}). \tag{4.7}$$

The fractions f_s and f_d do not necessarily add to unity because the magnitude of the power received from the specular reflectance is difficult to quantify. However, assuming that Equation 4.6 gives the correct model for the diffuse reflectance, f_d should approach unity as f_s approaches zero.

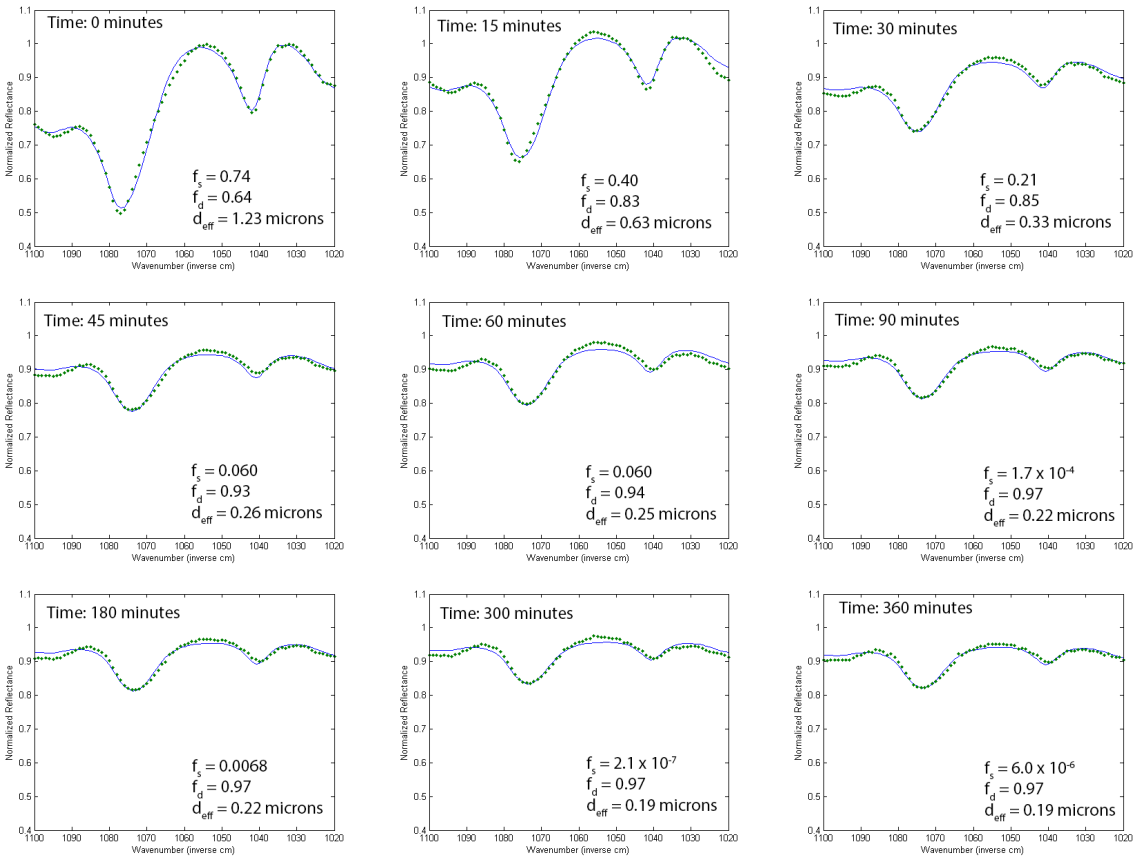

Figure 4.4: The time evolution of the reflectance spectra of DEP. The green dots are the experimental data, and the blue curve is the curve fitted using Equation 4.7. The fitted parameters are shown.

The blue curves in Figure 4.4 are the least-squares best-fit curves allowing the parameters f_s, f_d, and d_{eff} to vary. Note that all of the reflectance spectra are normalized to the reflectance spectrum of the clean brick. The curves fit the data very well, indicating that the above model of specular reflectance plus diffuse reflectance is a good model of the spectra.

Figure 4.5 shows the effective thickness (top) and specularity (bottom) as a function of time based on the best-fit curves. The specularity is defined to be

$$\frac{f_s}{f_s + f_d}. \tag{4.8}$$

As expected, the specular fraction decreases to zero as time progresses. The reason for this is that, as the DEP seeps into the brick, there are fewer and fewer liquid facets exposed on the surface. Thus, fitting a curve to the observed reflectance spectrum and analyzing the specular fraction could be a promising method for determining the surface film thickness. Since the specularity decreases as the liquid seeps into the substrate, the amount of time that it takes for the specularity to decrease to zero should be

inversely proportional to the porosity of the substrate and proportional to the viscosity of the liquid.

The top part of Figure 4.5 shows that the effective depth drops quickly to a small value, and then decreases much more slowly. This can be explained by the act that initially there is a relatively thick layer of DEP above the surface of the brick, all of which contributes to the effective depth. As the liquid seeps into the brick, the top layer disappears (which is why the specularity also disappears), and the underlying brick becomes soaked in liquid. The effective depth is then approximately half the average distance that light ravels through liquid inside the brick before escaping to the surface. Models for this phenomenon will be explored in the next section. Also note that f_d does not approach unity, but rather a value of approximately 0.97. This is indicative of index matching, which will also be discussed in the next section.

4.5 Modeling Diffuse Reflectance of Porous Materials

A porous material such as brick can be considered to be a collection of small particles similar to the bulk powders from Chapter 3. When a ray of light interacts with one of the particles, a portion of it is absorbed by the particle and a portion of it is scattered into a new direction. The ratio of the amount of light absorbed to the total amount of light that is either absorbed or scattered is the single-scatter albedo w. The scattered light then interacts with another particle and so on until eventually the light escapes from the porous material and contributes to the reflectance in the direction in which it escaped.

The direction into which the scattered ray propagates is determined by the scattering profile $p(g)$ where g is the angle between the incident direction and the scattered direction. For isotropically scattering particles, $p(g) = 1$. The scattering profile for spherical particles can be calculated using Mie Theory. However, it is often more useful to replace the scattering profile predicted by Mie Theory with the Henyey-Greenstein approximation [12]:

$$p(g) = \frac{1 - \xi}{(1 + 2\xi \cos(g) + \xi^2)^{3/2}}, \tag{4.9}$$

where ξ is the asymmetry parameter which can be calculated with Mie Theory. There are two advantages to the approach of calculating the asymmetry parameter with Mie Theory and then using the Henyey-Greenstein approximation rather than calculating the entire scattering profile with Mie Theory. The first is that it is computationally cheaper and the second is that it removes the fine structure present in Mie Theory which has a dubious relation to reality when particles are irregularly shaped and closely packed. Figure 4.6 shows a comparison of the scattering profiles for two particle sizes calculated with Mie Theory (blue) and the Henyey-Greenstein approximation (green).

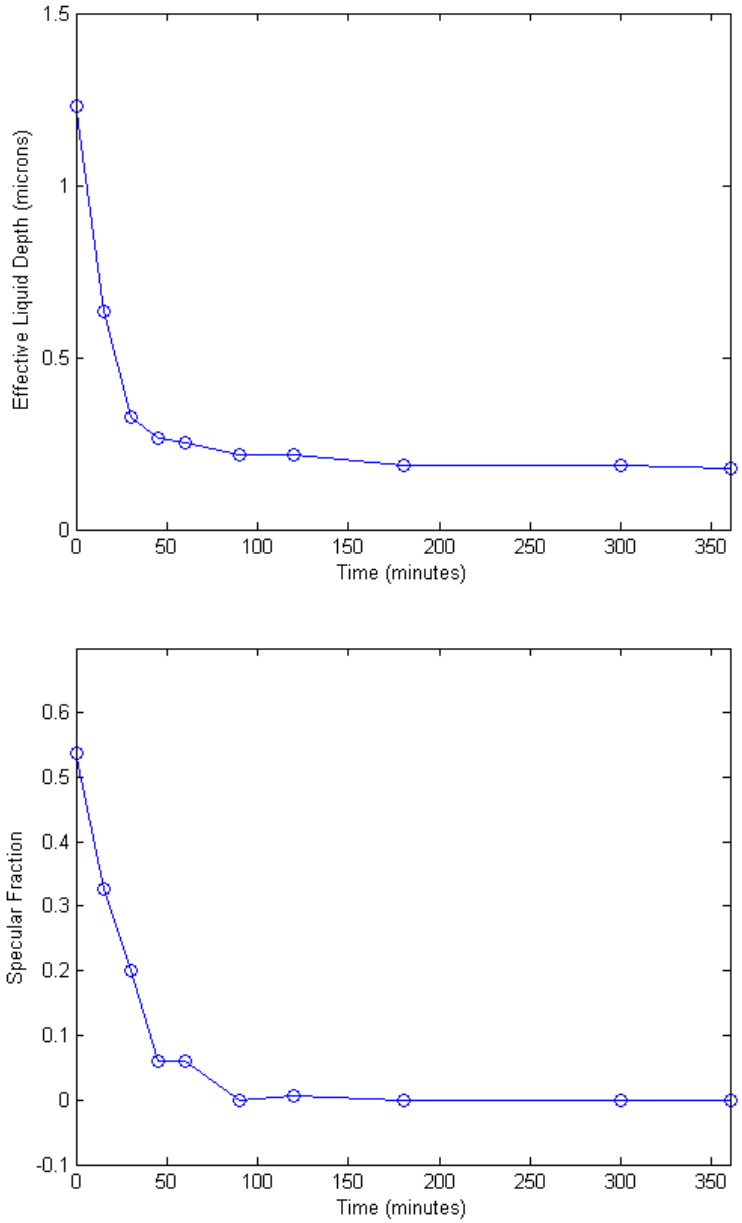

Figure 4.5: The effective depth (top) and specularity (bottom) as a function of time, as determined by the fitted parameters.

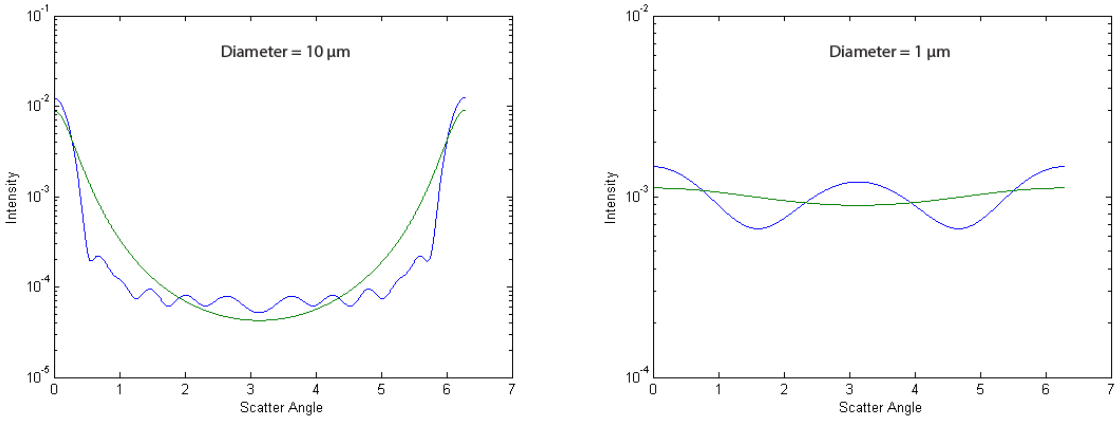

Figure 4.6: The Henyey-Greenstein function. The blue curve is the scattering profile calculated using Mie Theory and the green curve is the Henyey-Greenstein approximation. The refractive index of the particle is $2 + 2i$ and the wavenumber is $1000\,\mathrm{cm}^{-1}$. The left part of the figure is a $10\,\mu$m particle, and the right part of the figure is a $1\,\mu$m particle.

If the single-scatter albedo and the scattering profile are known, the reflectance as a function of angle can be calculated using a Monte Carlo method. The steps of the method are as follows:

- Propagate a ray a distance to an interaction site that is proportional to an exponential random number and inversely proportional to $S + A$, where S is the scattering coefficient and A is the absorption coefficient. An exponential random number is used because the exponential distribution is memoryless, that is, no matter how far the ray has traveled the probability that it will encounter a particle in the next moment in time is the same.
- Multiply the intensity of the ray by the single-scatter albedo, and then propagate the ray in a new direction determined probabilistically using the Henyey-Greenstein function
- Repeat the above two steps until a maximum number of scatter events is reached or until the ray escapes to the surface.
  - If the maximum number of scatter events is reached, the intensity of the ray is set to zero.
  - If the ray escapes to the surface, record the intensity and the angle relative to the surface normal.
- Repeat the above three steps N times, where N is the number of rays.
- Bin the rays into 100 equal intervals of emittance angle between 0 and $\frac{\pi}{2}$ to determine the reflectance as a function of emittance angle.

Appendix A.5 shows Matlab code that implements this algorithm.

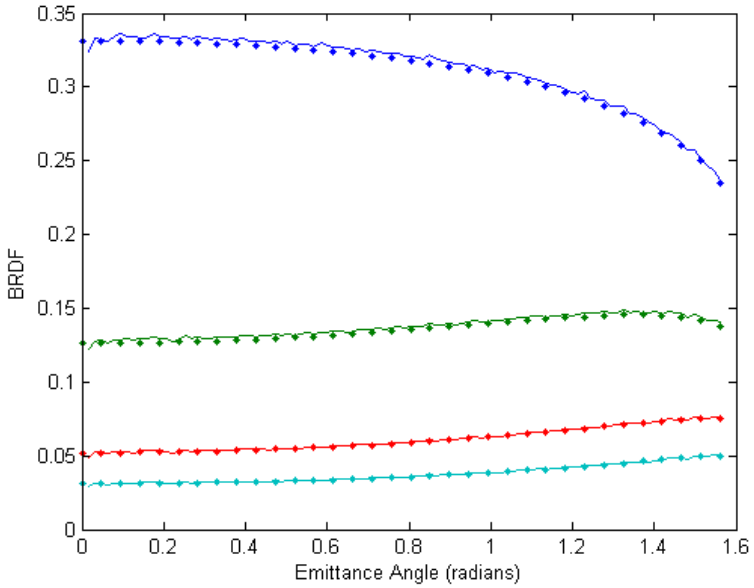

Figure 4.7: A comparison of the Monte Carlo method (solid lines) and the Hapke IMSA (dots) for single-scatter albedos of 1 (blue), 0.5 (green), 0.2 (red), and 0.1 (cyan).

For the case where the scattering profile is isotropic, this method gives the same results as the Hapke IMSA as expected. Figure 4.7 shows a comparison of the Monte Carlo method and the Hapke IMSA model.

However, the Monte Carlo simulation differs significantly from the Hapke IMSA model when the scattering profile is not isotropic as shown in figure 4.8. The scattering profiles were calculated using the Henyey-Greenstein function. The blue curve represents an asymmetry parameter of zero; the green curve represents an asymmetry parameter of 0.1; the red curve represents an asymmetry parameter of 0.5; and the cyan curve represents an asymmetry parameter of 0.9. As the asymmetry parameter increases, so too does the disagreement between the Monte Carlo method and the Hapke IMSA model. In particular, the reflectance at low angles of emittance decreases much more quickly as the asymmetry parameter increases.

An advantage of the Monte Carlo method is that it gives much more information about the interaction of light with the porous material than just the reflectance such as the depth of penetration into the material, as shown in Figure 4.9. The graph in the figure assumes nonabsorbing particles and the horizontal axis represents depth in multiples of the inverse of the scattering coefficient. The blue, green, and red curves represent asymmetry parameters of 0, 0.5, and 0.9 respectively. The vertical axis corresponds to the intensity of light relative to the intensity at the surface. As expected, the penetration depth increases as the asymmetry parameter increases. One possible way that information like this could be

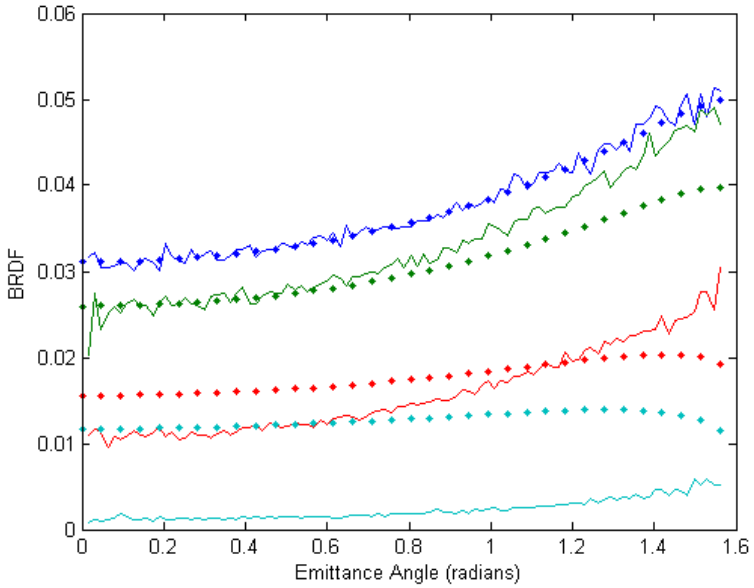

Figure 4.8: A comparison of the Monte Carlo method (solid lines) and the Hapke IMSA (dots) for a single-scatter albedo of 0.5. The asymmetry parameters are 0 (blue), 0.1 (green), 0.5 (red), and 0.9 (cyan).

useful for understanding the reflectance of wet porous materials is as follows: one could gather reflectance data of a particular material at many different angles, and then use the Monte Carlo method to model the material, allowing parameters such as the asymmetry parameter and particle size to vary. Then calculations of the penetration depth will give an estimate of the effective depth that light travels in the material which will allow estimation of the strength of the signal from an absorbing liquid contaminant.

One complication with this approach is that index-matching must be taken into account in some manner. Index-matching is the phenomenon where the reflectance/scattering properties of the particles in the porous material changes in the presence of the liquid because the refractive index of the liquid matches the refractive index of the porous material more closely than air does. Index-matching manifests itself in two ways. First, less light is reflected from each particle, which means that more light is absorbed, which causes the single-scatter albedo to decrease. Second, the asymmetry parameter usually increases (i.e., the particles become more forward-scattering). Both of these phenomena have the effect of reducing the reflectance that would otherwise be expected. Since the refractive index of the liquid is wavelength-dependent, index-matching is also wavelength-dependent, which means it can have a very complicated effect on the reflectance. However, if the liquid has weak absorption features (like DEP), the relative change in the refractive index is small and thus the effect of index-matching will be mostly wavelength-independent. The fact that the calculated spectra in Figure 4.4 match the experimental spectra so closely indicates that index-matching can be considered mostly a wavelength-independent phenomenon

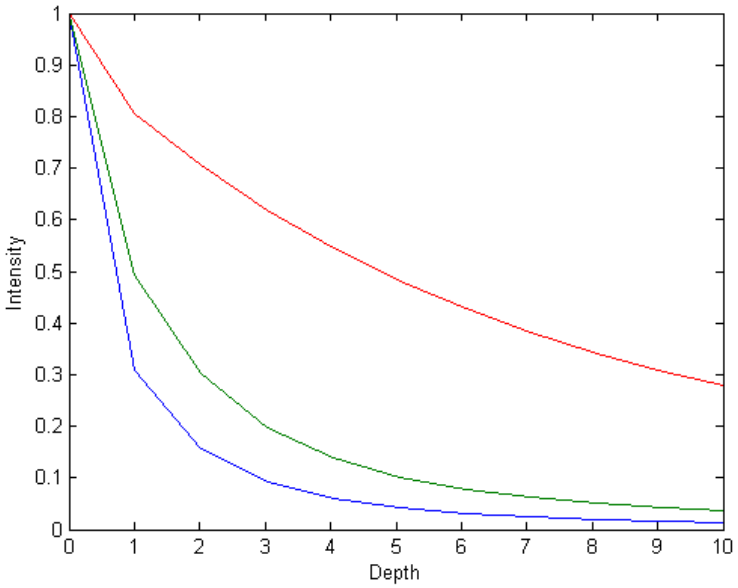

Figure 4.9: The intensity of light in the porous material as a function of the number of inverse scattering lengths for asymmetry parameters of 0 (blue), 0.5 (green), and 0.9 (red). The depth is in terms of multiples of the scattering coefficient.

in this case. Also note that the effect of index-matching in this case is small because $f_d = 0.97$ is very close to one. If the refractive index of the porous material is known or can be estimated, the effect of index-matching could possibly be calculated using Mie Theory.

Chapter 5

Speckle

5.1 Overview

Speckle is a phenomenon that is observed when coherent light reflects from a rough surface. Light incident on different parts of the rough surface travel slightly different distances to an observation plane, and a pattern of light and dark regions is formed in the observation plane due to interference of light amplitudes with random phases. Speckle is an inherent limiting factor in hyperspectral imaging because it is a source of noise that cannot be eliminated by increasing the power of the illumination source or the sensitivity of the camera. In this chapter, I discuss methods for reducing speckle contrast. I derive equations for the effect of spectral and angular diversity, and test them using simulations of speckle based on Fourier optics. Finally, I discuss how speckle is relevant to the case of sparse particles on a surface. Throughout the chapter, Goodman [6] is used as a reference, but I perform my own analysis.

5.2 Simulating Speckle

Speckle can be simulated using the methods of Fourier optics. Fourier optics makes the paraxial assumption that all rays propagate in nearly the same direction, and it also approximates the electric field as a scalar field. Thus, Fourier optics is valid when the polarization of the light does not change and the distance between the object and the camera lens is large relative to the aperture. Figure 5.1 shows a generic calculation of the intensity of light in an observation plane that is a distance z from the illumination plane. Appendix A.6 shows the Matlab function that was used for speckle simulation. We start with an $N \times N$ array of points representing the complex amplitude of the electric field in the illumination plane. The left image in Figure 5.1 shows the square of the magnitude of the complex amplitudes, which

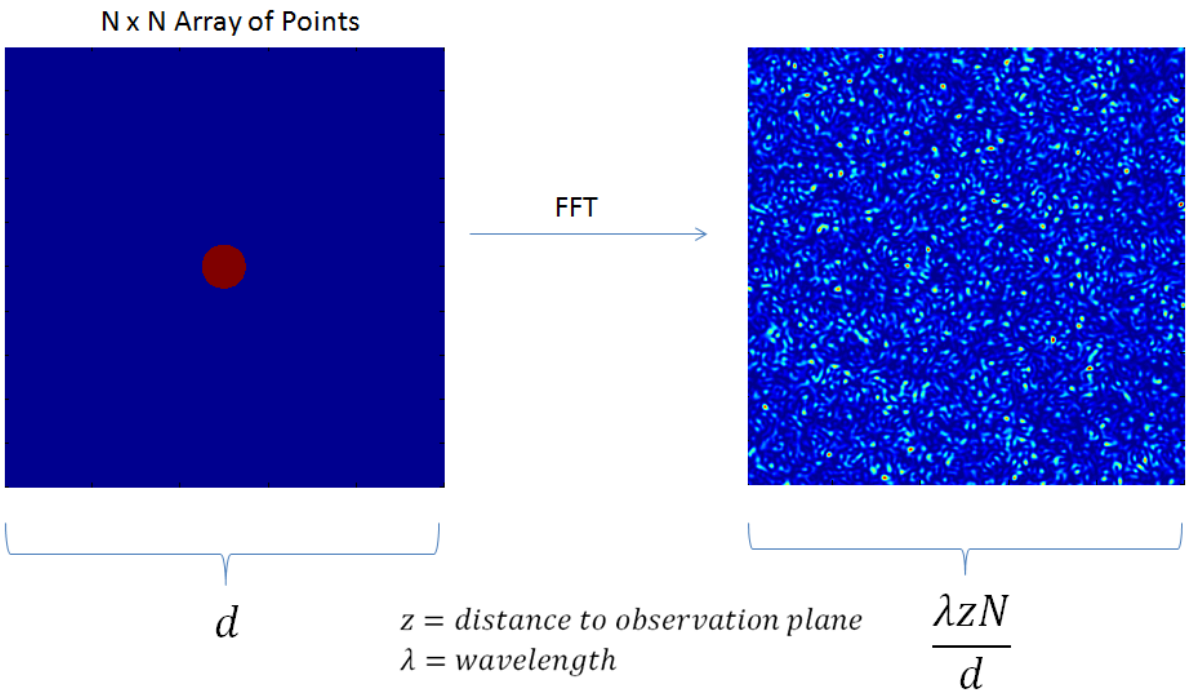

Figure 5.1: Simulating speckle patterns using FFT.

are constant within the illumination region shown in red. The phase of the amplitudes are randomly distributed within the illumination region. The amplitudes in a plane in the far field are calculated by taking the Fast Fourier Transform of the $N \times N$ array of points. If the physical width of the region represented by the $N \times N$ array was d, the physical width of the transformed region is $\frac{\lambda z N}{d}$.

In an imaging configuration, a Fourier transform operation has to be performed twice because the camera lens acts as a Fourier transform. Thus, the light is propagated to the aperture plane by taking a Fast Fourier Transform; then a mask is applied to the resulting array of points, representing the size of the aperture; and then another Fast Fourier Transform is applied to obtain the final complex amplitudes in the image plane. For the simulations in this section, it is assumed for simplicity that the entire field of view is illuminated. It is also assumed that the surface is delta-correlated, i.e., that the correlation length of the surface height variations is small enough that the phase of one point in the $N \times N$ array is not correlated with the phase of the neighboring points (at least for the random part of the phase; phase shifts due to sample orientation, for instance, are obviously correlated).

5.3 Speckle Contrast

The intensity of a speckle pattern is exponentially distributed; thus, a speckle pattern produced by monochromatic light that remains perfectly polarized will have an intensity pattern in the observation plane such that the standard deviation of the intensity is equal to the mean intensity. In real imaging systems, however, there are finite apertures, pixel sizes, and spectral widths which cause the variation in intensity to decrease. A useful number for characterizing the variation in intensity on a pixel-by-pixel basis is the contrast, which is defined as the standard deviation of the intensity observed in each pixel divided by the mean intensity (equivalently, the contrast is the reciprocal of the signal to noise ratio). The contrast is given by

$$C = \frac{1}{\sqrt{M}}, \tag{5.1}$$

where M is a parameter representing degrees of freedom. For fully developed speckle with no speckle averaging, $M = 1$. In this chapter, I consider five factors related to speckle averaging which contribute to M in an imaging configuration: 1) spatial, 2) polarization, 3) spectral, 4) angular, and 5) temporal. The total value for M is equal to the product of the degrees of freedom contributed by each of the above factors:

$$M = M_{spatial} M_{polarization} M_{spectral} M_{angular} M_{temporal}. \tag{5.2}$$

5.4 Spatial Diversity

If the illuminated region is much larger than the projected resolution cell of the camera, the size of the speckles in the imaging plane of the camera is equal to the size of the point spread function due to diffraction by the circular aperture of the lens. Speckle averaging occurs when multiple speckles lie within a single pixel area $A_{pix} = d_{pix}^2$. The diffraction-limited spot size at the imaging plane is given by

$$d_{diffraction} = \frac{\lambda}{D_{lens}} \frac{1}{1 - \frac{d}{f}} \approx \frac{\lambda f}{D_{lens}}, \tag{5.3}$$

where the approximation is valid for $d >> f$. For a circular aperture, the area of the diffraction-limited spot is

$$A_{speckle} = \frac{4}{\pi} d_{diffraction}^2. \tag{5.4}$$

Figure 5.2 demonstrates the effect of f-number on speckle size. The images were taken at $1000\,\mathrm{cm}^{-1}$. The top image has an f-number of 4; the middle image has an f-number of 10; and the bottom image has an f-number of 20.

The degrees of freedom parameter $M_{spatial}$ depends on the ratio of the pixel area to the speckle area, $\mathcal{R} = \frac{A_{pix}}{A_{speckle}}$. Reference [13] gives the exact expression for $M_{spatial}$ assuming a lens with a Gaussian aperture; the calculation is easier than for a circular lens and the result is nearly the same:

$$M_{spatial} = \left[\sqrt{\frac{1}{\mathcal{R}}}\,\mathrm{erf}\left(\sqrt{\pi\mathcal{R}}\right) - \left(\frac{1}{\pi\mathcal{R}}\right)\left(1 - \exp\left[-\pi\mathcal{R}\right]\right)\right]^{-2}. \tag{5.5}$$

When the pixel size is larger than the speckle size, $M_{spatial}$ is approximately equal to $1+\mathcal{R}$. Figure 5.3 shows a comparison of $M_{spatial}$ calculated using Equation 5.3 and $M_{spatial}$ calculated using a simulation with a circular aperture as described in Section 5.2.

Figure 5.4 shows a simulation of the speckle pattern on the image plane for $\lambda = 10\,\mu$m and $\frac{f}{D_{lens}} = 1$. The plots show the simulated reflectance spectrum at a single pixel from a rough surface having a uniform reflectance. As expected, the speckle noise decreases considerably as the pixel size increases.

5.5 Polarization Diversity

When the light scattered from the rough surface is depolarized, the intensity observed in the image plane will essentially be the sum of two partially independent speckle patterns, where the degree of independence depends on the degree of polarization. The expression for $M_{polarization}$ is

$$M_{polarization} = \frac{2}{1+P^2}, \tag{5.6}$$

where P is the polarization. Greater depolarization is expected for volume scattering in bulk powders because there are many complicated scattering events involved. However, it can be seen from the equation that depolarization can at best decrease the speckle contrast by a factor of $\sqrt{2}$, so polarization averaging has only a minor effect on speckle.

5.6 Spectral Diversity

As the wavelength of illumination is changed, the speckle pattern in the image plane also changes. The magnitude of the change is related to the round-trip optical path-length difference (OPD) of light within an optical resolution element of the lens. The size of a resolution element at the object is approximately

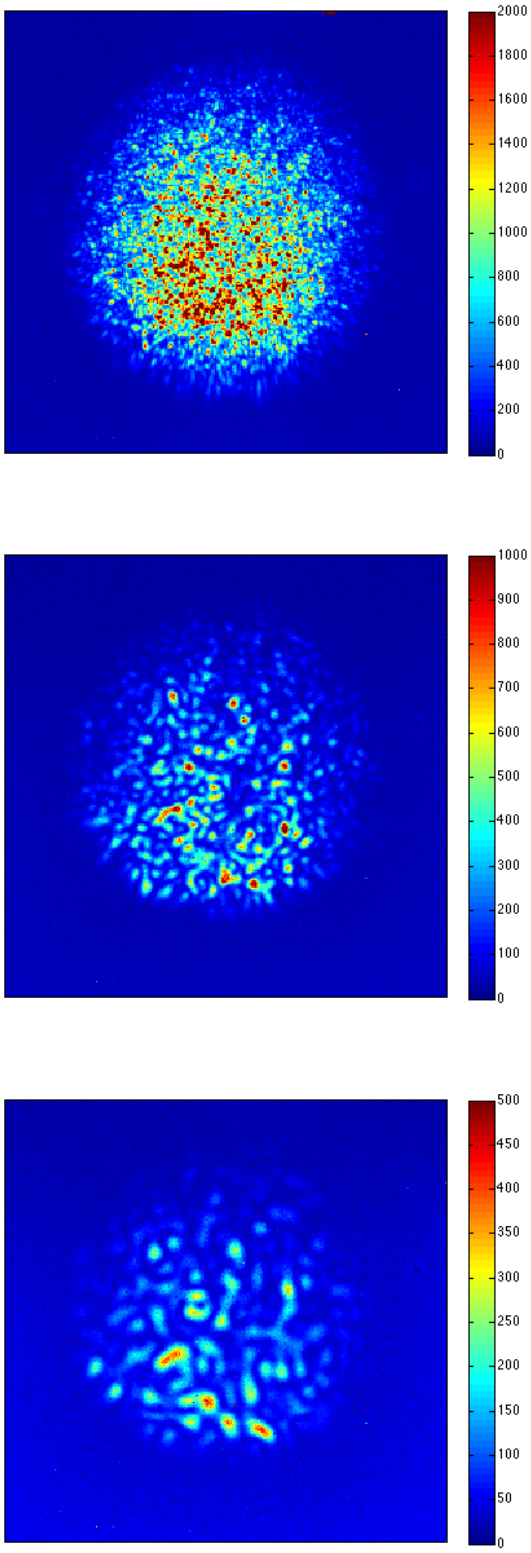

Figure 5.2: Images of speckle from diffuse gold at $1000\,\mathrm{cm}^{-1}$. The top image is an f/4 aperture; the middle image is an f/10 aperture; and the bottom image is an f/20 aperture.

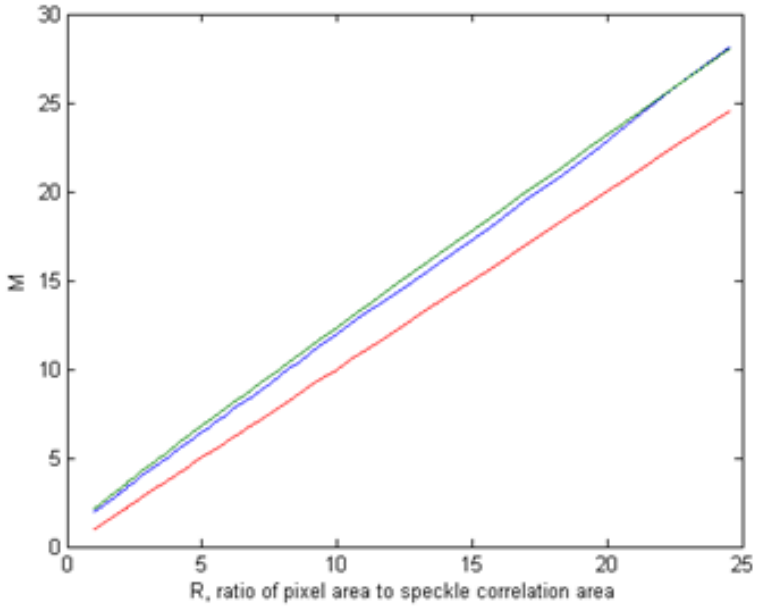

Figure 5.3: $M_{spatial}$ as a function of the ratio of pixel area to speckle correlation area. The blue curve represents a numerical simulation with a circular aperture, the green curve represents the exact solution given in Equation 5.5 for a Gaussian aperture, and the red curve represents the approximation $M_{spatial} = R$.

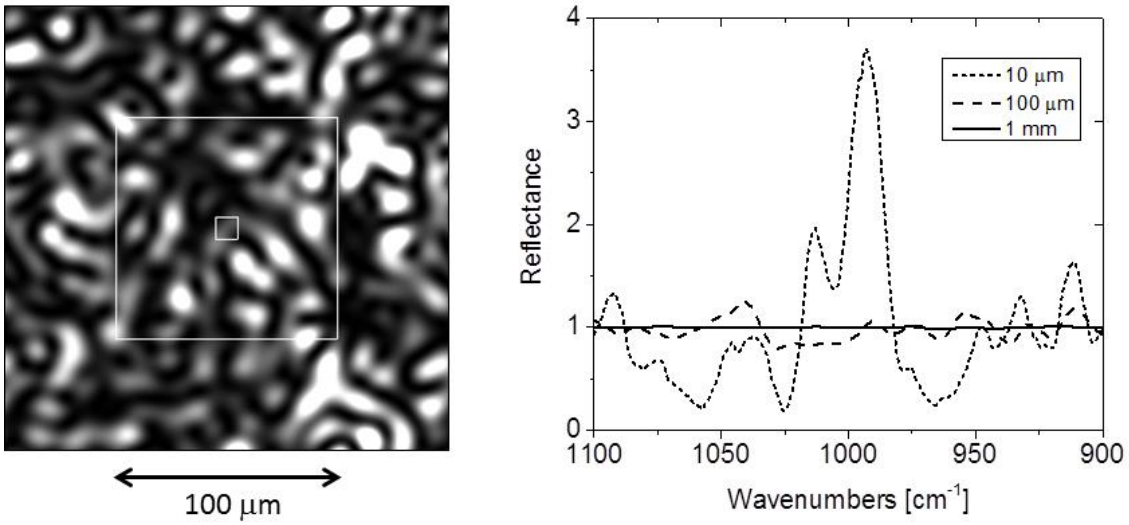

Figure 5.4: Simulation of spectra for various pixel sizes and an f-number of 1. It was assumed that the surface is uniformly reflective.

given by $\frac{d\lambda}{D_{lens}}$. The greater the OPD within a resolution element, the more the speckle pattern will change as the laser wavelength is changed. I will consider two factors which contribute to the OPD: 1) viewing the object surface at a non-normal angle, and 2) random height variations of the object. Of course, if there weren't random height variations on the object, then there would be no speckle pattern in the first place, so the second factor is always present; however, at large viewing angles or large distances, the first factor can dominate. In the following discussion, it will be assumed that for simplicity that the laser angle is zero, so that the only angle of concern is the viewing angle (i.e., the sample angle).

First consider the effects of a non-normal viewing angle. I will derive an expression for $M_{spectral}$ due to non-normal viewing angle using equations given in References [6] and [13]. The generic formula for M given in Reference [6] is

$$M = \left[\int_{-\infty}^{\infty} K_G\left(\Delta\widetilde{\nu}'\right) \left|\mu\left(\Delta\widetilde{\nu}'\right)\right|^2 \mathrm{d}\Delta\widetilde{\nu}' \right]^{-1}, \tag{5.7}$$

where $K_G(\Delta\widetilde{\nu}')$ is the autocorrelation function of the normalized power spectrum $G(\Delta\widetilde{\nu}')$, and $\mu(\Delta\widetilde{\nu}')$ is the amplitude autocorrelation function of the speckle pattern. If we assume a top-hat (i.e., uniformly distributed) power spectrum, then

$$G(\Delta\widetilde{\nu}') = \frac{1}{\Delta\widetilde{\nu}'}, \qquad -\frac{\Delta\widetilde{\nu}}{2} < \Delta\widetilde{\nu}' < \frac{\Delta\widetilde{\nu}}{2}, \tag{5.8}$$

where $\Delta\widetilde{\nu}$ is the bandwidth. Then

$$K_G(\Delta\widetilde{\nu}') = \frac{1}{\Delta\widetilde{\nu}} \Lambda\left(\frac{\Delta\widetilde{\nu}'}{\Delta\widetilde{\nu}}\right), \tag{5.9}$$

where Λ is the triangle function.

According to Reference [13], the autocorrelation function of speckle patterns in an imaging configuration as a function of wavenumber is given by the normalized area overlap between the two shifted apertures. If the observation/illumination angle is θ, then the amount that a speckle pattern shifts when the wavenumber is changed by an amount $\Delta\widetilde{\nu}'$ is $2\lambda d \tan(\theta)\Delta\widetilde{\nu}'$. Thus, if we assume a square aperture with side lengths d_{lens} (the math is easier with a square aperture than with a circular aperture), then

$$\begin{aligned} \mu(\Delta\widetilde{\nu}') &= \Lambda\left(\frac{\Delta\widetilde{\nu}'}{\Delta\widetilde{\nu}_0}\right), \\ \Delta\widetilde{\nu}_0 &= \frac{D_{lens}}{2\lambda d \tan(\theta)}. \end{aligned} \tag{5.10}$$

We can call the parameter $\Delta\widetilde{\nu}_0$ the characteristic bandwidth; it represents the change in wavenumber needed to shift the speckle pattern in the aperture plane by one aperture diameter, causing the speckle pattern in the image plane to completely decorrelate.

Now, substituting Equations 5.9 and 5.10 into Equation 5.7,

$$\begin{aligned} M &= \left[\int_{-\infty}^{\infty} \frac{1}{\Delta\widetilde{\nu}} \Lambda\left(\frac{\Delta\widetilde{\nu}'}{\Delta\widetilde{\nu}}\right) \left|\Lambda\left(\frac{\Delta\widetilde{\nu}'}{\Delta\widetilde{\nu}_0}\right)\right|^2 \mathrm{d}\Delta\widetilde{\nu}'\right]^{-1} \\ &= \left[2\int_0^{\min(\Delta\widetilde{\nu},\Delta\widetilde{\nu}_0)} \frac{(\Delta\widetilde{\nu}-\Delta\widetilde{\nu}')}{\Delta\widetilde{\nu}} \frac{(\Delta\widetilde{\nu}_0-\Delta\widetilde{\nu}')^2}{\Delta\widetilde{\nu}_0^2}\,\mathrm{d}\Delta\widetilde{\nu}'\right]^{-1}. \end{aligned} \tag{5.11}$$

Solving this integral for the two cases $\Delta\widetilde{\nu} < \Delta\widetilde{\nu}_0$ and $\Delta\widetilde{\nu} > \Delta\widetilde{\nu}_0$:

$$M_{spectral} = \begin{cases} \left(1 - \frac{2\Delta\widetilde{\nu}}{3\Delta\widetilde{\nu}_0} + \frac{\Delta\widetilde{\nu}^2}{6\Delta\widetilde{\nu}_0^2}\right)^{-1}, & \frac{\Delta\widetilde{\nu}}{\Delta\widetilde{\nu}_0} < 1 \\ \left(\frac{2\Delta\widetilde{\nu}_0}{3\Delta\widetilde{\nu}} - \frac{\Delta\widetilde{\nu}_0^2}{6\Delta\widetilde{\nu}^2}\right)^{-1}, & \frac{\Delta\widetilde{\nu}}{\Delta\widetilde{\nu}_0} > 1 \end{cases} \tag{5.12}$$

In the limit of large $\frac{\Delta\widetilde{\nu}}{\Delta\widetilde{\nu}_0}$, $M_{spectral} \approx \frac{3}{2}\frac{\Delta\widetilde{\nu}}{\Delta\widetilde{\nu}_0}$. The above equation is validated by Figure 5.5, which shows a comparison of $M_{spectral}$ calculated with Equation 5.12 and $M_{spectral}$ calculated from simulations of speckle. The slight discrepancy in the curves can be accounted for by two factors: first, the above derivation implicitly assumed that the change in wavenumber $\Delta\widetilde{\nu}$ is small compared to the wavenumber. Secondly, the derivation assumed a rectangular aperture, whereas the simulation assumed a circular aperture.

Now consider the second source of spectral averaging: random variations in the height of the surface. The roughness of a Gaussian surface can be characterized by the standard deviation in height, σ_h. As σ_h increases, the difference in phase between scattered light of two different wavelengths also increases. This means that the speckle patterns produced by the two wavelengths become decorrelated. When the spectral width $\Delta\widetilde{\nu}$ is large compared with σ_h, many decorrelated speckle patterns are added together, resulting in a reduction of the observed contrast. Reference [13] gives the expression for $M_{spectral}$ assuming a Gaussian-distributed power spectrum with standard deviation $\Delta\widetilde{\nu}$:

$$M_{spectral} = \sqrt{1 + 2\pi^2\sigma_h^2\Delta\widetilde{\nu}^2}. \tag{5.13}$$

If, instead, we consider the case where the power spectrum is top-hat distributed, a derivation similar to the one above gives a new characteristic bandwidth

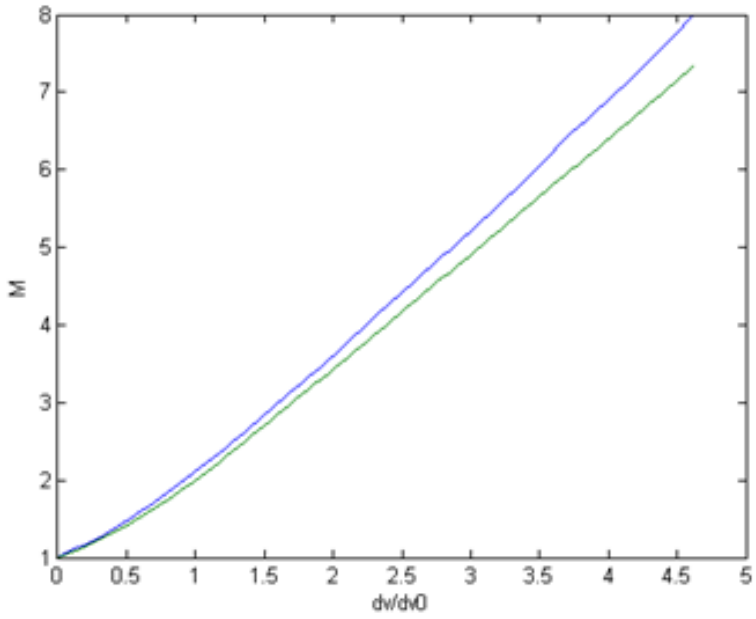

Figure 5.5: $M_{spectral}$ as a function of $\frac{\Delta\widetilde{\nu}}{\Delta\widetilde{\nu}_0}$. The blue curve represents a numerical simulation performed with $d_{lens} = 0.625cm, \lambda = 10\,\mu\text{m}, D = 100cm, and\theta = 30°$. The green curve was calculated using equation 5.12.

$$\Delta\widetilde{\nu}_0 = \frac{1}{4\pi\sigma_h}. \tag{5.14}$$

Unlike in the case of the non-normal viewing angle, this characteristic bandwidth represents the change in wavenumber needed to decorrelate the speckle pattern by a factor of e. The correlation will never go to zero because the surface height variation is Gaussian distributed. In the limit of large $\frac{\Delta\widetilde{\nu}}{\Delta\widetilde{\nu}_0}$,

$$M_{spectral} \approx \frac{1}{\pi}\frac{\Delta\widetilde{\nu}}{\Delta\widetilde{\nu}_0}. \tag{5.15}$$

There are at least two approaches to overcoming speckle when considering spectral diversity. Choosing a configuration in which the spectral region of interest is small compared with the characteristic bandwidth $\Delta\widetilde{\nu}_0$ (i.e., the object is close, the observation angle is small, or the surface height variations are small) means that the shape of the reflectance spectra within a single pixel will not change very much. However, the pixel-to-pixel variation in the received power could be very large, and in some of the pixels the power might be too low for detection to occur. Making the aperture diameter as large as possible is advantageous in this case. On the other hand, one might wish to operate in the regime where the spectral region of interest is much larger than $\Delta\widetilde{\nu}_0$ (i.e., the object is far away, the observation angle

is large, or the surface height variations are large)/ In this case, one can average over many different wavelengths to reduce the speckle contrast. Also, if decorrelation of the speckle patterns occurs due to a non-normal observation angle, then *decreasing* the aperture diameter can be advantageous because it allows for greater spectral averaging at the expense of received power and spatial resolution.

In determining which approach to use, it is useful to know the correlation between two speckle patterns in the image plane generated by two different wavelengths. In the case where the decorrelation of the speckle patterns is caused solely by the surface height variations, the correlation between two speckle patterns produced by wavenumbers which differ by $\Delta\widetilde{\nu}$ is given by

$$\rho = \exp\left[-\left(\frac{\Delta\widetilde{\nu}}{\Delta\widetilde{\nu}_0}\right)^2\right], \tag{5.16}$$

where $\Delta\widetilde{\nu}_0 = \frac{1}{4\pi\sigma_h}$ as before. The average spectral separation of the peaks in the observed spectrum which arise due to speckle is approximately $1.3\Delta\widetilde{\nu}_0$ (Reference [23]). For example, in Figure 5.4, $1.3\Delta\widetilde{\nu}_0 = \frac{1.3}{4\pi(100\,\mu\mathrm{m})} = 10\,\mathrm{cm}^{-1}$, and the actual average peak separation for the smallest pixel size is $10\,\mathrm{cm}^{-1}$.

In the case where the decorrelation of the speckle patterns is caused by a non-normal viewing angle, the correlation between two speckle patterns produced by wavenumbers which differ by $\Delta\widetilde{\nu}$ is

$$\rho = 1 - \frac{\Delta\widetilde{\nu}}{\Delta\widetilde{\nu}_0}, \tag{5.17}$$

where $\Delta\widetilde{\nu}_0 = \frac{D_{lens}}{2\lambda d\tan(\theta)}$. This equation is valid for $\Delta\widetilde{\nu} < \Delta\widetilde{\nu}_0$; for $\Delta\widetilde{\nu} > \Delta\widetilde{\nu}_0$, the correlation is zero because the speckle pattern in the aperture plane will have shifted by more than one aperture diameter.

5.7 Angular Diversity

Reduction in speckle contrast through angular diversity is very similar to reduction in speckle contrast through spectral diversity at a large observation angle. Both cases involve shifting the speckle pattern in the aperture plane relative to the aperture. In the case of spectral diversity, the speckle pattern in the aperture plane shifts as the wavenumber changes; in the case of angular diversity, either the speckle pattern can shift as the sample rotates or the aperture itself can shift to view the sample at different angles. Similar to the characteristic bandwidth, we can define a characteristic "tangent width" which is the change in the tangent of the observation angle that will move the speckle pattern relative to the aperture by one aperture diameter. This characteristic tangent width, just like the characteristic bandwidth, is also proportional to the ratio of the aperture diameter to the object distance:

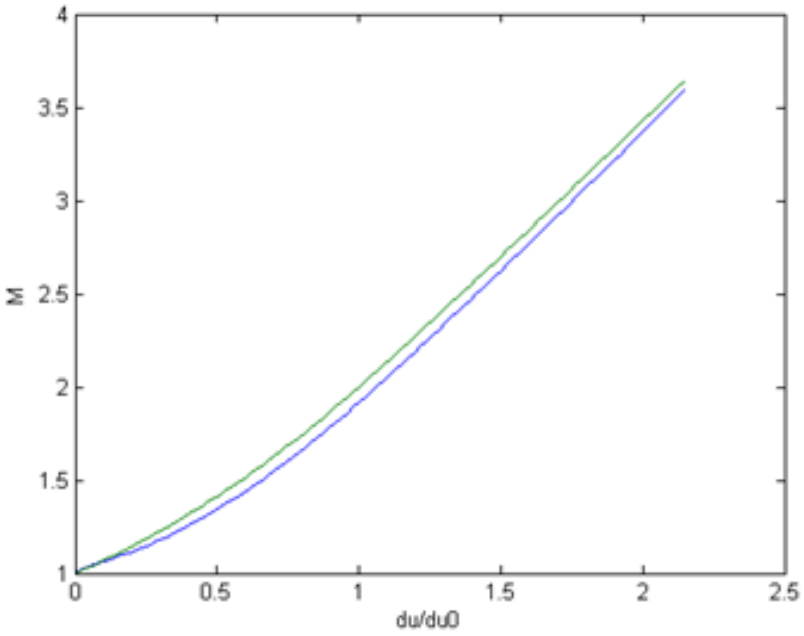

Figure 5.6: $M_{angular}$ as a function of $\frac{\Delta u}{\Delta u_0}$. The blue curve is a numerical simulation with $d = 10cm$ and $D_{lens} = 2.5cm$. The observation angles ranged from 0 degrees to 15 degrees. The green curve was calculated using Equation 5.19.

$$\Delta u_0 = \frac{D_{lens}}{2d}, \tag{5.18}$$

where $u = \tan\theta$. Now an equation similar to equation 5.12 can be derived using the same method as in the above section to give the degrees of freedom $M_{angular}$ associated with averaging over all observation angles between θ_1 and θ_2:

$$M_{angular} = \begin{cases} \left(1 - \frac{2\Delta u}{3\Delta u_0} + \frac{\Delta u^2}{6\Delta u_0^2}\right)^{-1}, & \frac{\Delta u}{\Delta u_0} < 1 \\ \left(\frac{2\Delta u_0}{3\Delta u} - \frac{\Delta u_0^2}{6\Delta u^2}\right)^{-1}, & \frac{\Delta u}{\Delta u_0} > 1 \end{cases} \tag{5.19}$$

$$\Delta u = \left|\tan(\theta_2) - \tan(\theta_1)\right|. \tag{5.20}$$

Figure 5.6 shows a comparison of $M_{angular}$ calculated with the above equation and calculated from simulated speckle patterns. The curves match very closely; the small discrepancy can be attributed to the fact that the above equation was derived under the assumption of a square aperture, whereas the simulations used a circular aperture.

5.8 Temporal Diversity

Temporal diversity can be achieved by varying in time the phase of the light incident on each point of the surface, so that different speckle patterns are realized at different moments in time. A common method for speckle contrast reduction through temporal diversity is to place a moving diffuser and a stationary diffuser in front of the illumination source. In Reference [2], for instance, two polycrystalline diamond plates were used. The stationary diffuser ensures that the illumination has a uniform distribution of phases, and the moving diffuser scrambles those phases in time. If the moving diffuser moves with a speed v and has a phase correlation radius r_0, then according to Reference [6],

$$M_{temporal} \propto \frac{vT}{r_0}, \tag{5.21}$$

where T is the integration time and the proportionality constant is a function of the standard deviation of the change in phases imparted by the diffuser system.

The tradeoff with using this method to achieve temporal diversity is that it increases the divergence of the illumination source, which restricts the standoff distance of the hyperspectral imaging system.

5.9 Partially Developed Speckle and Fill Factor

In all of the discussions above, it was assumed that the speckle was fully developed; that is, the phase of the reflected light has a uniform phase distribution over the full range from 0 to 2π. It was also assumed that the surface was uniformly illuminated and the magnitude of the reflectance was the same everywhere on the surface. However, when dealing with trace particles on a smooth surface, for instance, both of these assumptions can become invalid.

First consider the illumination of a single particle, with a size on the order of the wavelength of smaller. The "speckle lobes" produced by such a particle are essentially the lobes described by Mie Theory, or some other much more complicated theory in the case of an irregularly shaped particle. Since the purpose of discussing speckle is to understand how the reflectance spectrum will vary relative to the "true" reflectance spectrum, it is not useful to describe a single particle in terms of speckle; whatever model is used to describe the reflectance spectrum as a function of angle will naturally incorporate "speckle" into the calculation. On the other hand, for an irregularly shaped particle that is much larger than the wavelength (but still smaller than the spatial resolution of the camera), it can be useful to view the reflectance from such a particle as a uniform reflectance from a region of a rough surface whose area is the same as the cross section of the particle. There are two things to note about this case: first,

since the particle is small relative to the spatial resolution of the camera, the size of the speckle lobes produced by this particle in the aperture plane will be much larger than what has been assumed in the above discussions. In particular, the width of a speckle lobe in the aperture plane is [13], [6]

$$\delta x = \frac{\lambda d}{D}, \tag{5.22}$$

where d is the distance from the surface to the aperture plane and D is the diameter of the particle. Since the speckle lobes are so large, the shape of the reflectance spectrum will not change very much due to speckle. However, the power received by the pixel onto which the particle is imaged can vary depending on whether the aperture happens to be in a low point of the speckle pattern or a high point. The second thing to note about this case is that, if the irregularities on the surface of the particle are not large compared with the wavelength, then the speckle pattern will be only partially developed. This results in a reduction in contrast because the full range of phases is not available for interference. If N_{facets} is the number of individual facets that reflect light from the particle, and σ_ϕ is the standard deviation of the phase of the light that is reflected from each facet, then the contrast of the partially developed speckle produced by the particle is approximately

$$C = 2\sqrt{\frac{2}{N_{facets}}}\sinh\left(\frac{\sigma_\phi^2}{2}\right) \tag{5.23}$$

This equation is only valid for $\sigma_\phi << 2\pi$.

Now consider the case where there are sparse particles within a spatial resolution cell of the camera (i.e., the fill factor is small). We will assume that the particles are either very small or that their surfaces are smooth enough that the phase of the light reflected from each particle has a very narrow distribution, and we will also assume that the phase of the light reflected from each particle is randomly distributed between 0 and 2π. As the number of particles increases, the speckle pattern will closer to a fully developed speckle pattern. If $N_{particles}$ is the number of particles within a spatial resolution cell, the degrees of freedom associated with the fill factor is

$$M_{fill} = \frac{N}{N-1}. \quad [6]. \tag{5.24}$$

Thus, we can see from this equation that a small fill factor will only decrease the speckle contrast if there are a very small number of particles in each resolution cell. This is one reason why speckle can be less of a problem at short distances than at long distances.

Chapter 6

Conclusions

The feasibility of hyperspectral imaging for the detection of particles on surfaces was demonstrated using potassium chlorate particles on car panels at distances of 5 m, 10 m, and 20 m. Using the Adaptive Cosine Estimation (ACE) algorithm, the potassium chlorate fingerprints were easily visible at many different sample angles. However, in general, there is a large amount of variation in the shape and magnitude of spectra in a hyperspectral image that depend on factors such as particle size, viewing geometry, and surface reflectivity. Mie Theory calculations performed on simulated materials, combined with information from sources such as Hapke [4], gave qualitative insight into the expected shape and magnitude of reflectance spectra from sparse particles on a surface. The shape of the spectra depends on whether the particles are strongly absorbing or weakly absorbing. Strongly absorbing particles tend to have reflectance maxima near the resonant frequency, whereas weakly absorbing particles tend to have reflectance minima. For highly reflective substrates, the reflectance decreases sharply as the sample angle increases and becomes more dominated by backward scattering, which has a flatter spectrum around the Christiansen frequency. The double interaction model, which uses Mie Theory to calculate the contributions to the reflectance along two different light paths, accurately accounted for how the shape and magnitude of the reflectance spectra of sodium chlorate particles on gold and silica surfaces changed as a function of sample angle and laser angle. This suggests that the double interaction model could be combined with advanced knowledge of a target to calculate an improved reference spectrum to be used with the ACE algorithm.

A method for approximating the mean particle size based on the location of the peak near the Christiansen frequency was derived. This method, when applied to the sodium chlorate sample, yielded a result for the mean particle diameter that was approximately half of the value determined using a microscope.

The Hapke Isotropic Multiple Scattering Approximation (IMSA), combined with Mie Theory, gave qualitative insight into the expected shape and magnitude of reflectance spectra from bulk powders. Compared with the reflectance spectra from sparse particles, the spectra from bulk powders are much simpler and less dependent on the viewing geometry. The Hapke IMSA model was able to accurately account for the observed changes in the reflectance from bulk sodium chlorate powder at multiple sample angles and laser angles.

A final scenario of interest was thin films on rough or porous surfaces. Using a model that takes into account diffusely reflected and specularly reflected light, the observed reflectance spectra from diethyl phthalate (DEP) on a brick was fitted to a high degree of accuracy. This suggests a promising method for using hyperspectral imaging to determine the thickness of liquids on porous surfaces.

Finally, the issue of speckle in hyperspectral imaging was examined using simulations based on Fourier optics and information from sources such as Goodman [6]. Speckle is a limiting factor in hyperspectral imaging because it is noise that scales with the signal, and thus cannot be eliminated by increasing the signal strength. The speckle noise can only be reduced by averaging multiple uncorrelated speckle patterns. Equations from various sources were presented that describe the reduction in speckle contrast for spatial, spectral, polarization, temporal, and angular averaging. Original equations for the reduction in contrast for spectral and angular averaging were derived.

Appendix A

Matlab and C++ Code

A.1 Mie Theory Particle Distribution

The following Matlab function calculates the BRDF for a distribution of particles with radii given by the array a and number of particles of each radius given by $coeffs$. The array v is the list of wavenumbers, N is the complex refractive index at each wavenumber, $Theta$ is the laser angle, and p is the polarization.

```
function r = distributionBRDF(v, N, a, coeffs, Theta, p)
    r = 0;
    for ii = 1:length(a)
        disp(ii);
        output = scatterMieElectricField(v, N, a(ii), Theta, p, 1);
        r = r + coeffs(ii)*sum(abs(output).^2);
    end
    areaSum = sum(coeffs*pi.*a.^2);
    r = r/areaSum;
end

function Output = scatterMieElectricField(v, N, a, Theta, p, d)
    %d is distance away from particle at which measurement is made
    %p is polarization angle (pi/2 is vertical, 0 is horizontal)
    E = ones(2, length(v));
    for ii = 1:length(v)
        if length(Theta) > 1
            result = Mie_S12(N(ii), 2*pi*v(ii)*a, cos(Theta(ii)));
        else
            result = Mie_S12(N(ii), 2*pi*v(ii)*a, cos(Theta));
        end
        S1 = result(1);
        S2 = result(2);
        E(1,ii) = exp(1i*2*pi*v(ii)*d)/1i/2/pi/v(ii)/d*S1*sin(p);
        E(2,ii) = -exp(1i*2*pi*v(ii)*d)/1i/2/pi/v(ii)/d*S2*cos(p);
    end
    Output = E;
end
```

A.2 Sphere on Surface

The following C++ code uses the SCATMECH library developed by NIST to calculate the BRDF of a sphere on a surface. The function *bobbertVlieger* uses the exact Bobbert Vlieger equations, and the function *doubleI* uses the double interaction model.

```
#include "bobvlieg.h"
#include "sphprt.h"
#include "miescat.h"
#include <iostream>
#include <fstream>
#include <vector>
#include <string>
#define _USE_MATH_DEFINES
#include <math.h>
#include "diffuse.h"
#include "filmtran.h"
#include "brdf.h"
#include "lambert.h"

using namespace std;          // Use unqualified names for Standard C++
    library
using namespace SCATMECH;     // Use unqualified names for the SCATMECH
    library

int bobbertVlieger()
{
        double thetai = 10*M_PI/180;
        double theta = 10*M_PI/180;
        double phi = 180*M_PI/180;

    Bobbert_Vlieger_BRDF_Model model;

        model.AskUser();
        //dielectric_function theIndex;
        //theIndex.read("SilicaRefractiveIndex.txt");
        //model.set_n2(theIndex);
        //theIndex.read("SilicaRefractiveIndex.txt");
        //model.set_substrate(theIndex);

        vector<double> v;
        double startWN = 900;
        double endWN = 1100;

        for (double i=startWN;i<=endWN;i+=2) {
                v.push_back(i);
        }

        ofstream myfile;
        myfile.open("outputFile0.csv");

        for (int i=0; i<v.size(); i++) {
```

```
                cout << endl << i << endl;

                model.set_lambda(10000/v[i]);

                complex<double> jonespp = model.Epp(thetai,theta,phi);
                complex<double> jonesps = model.Eps(thetai,theta,phi);
                complex<double> jonessp = model.Esp(thetai,theta,phi);
                complex<double> jonesss = model.Ess(thetai,theta,phi);

                myfile <<
                v[i] << "," <<
                real(jonespp) << "," << imag(jonespp) << "," <<
                real(jonesps) << "," << imag(jonesps) << "," <<
                real(jonessp) << "," << imag(jonessp) << "," <<
                real(jonesss) << "," << imag(jonesss) << endl;
        }

        myfile.close();

        std::cout << "Enter something to exit\n";
    char sTemp[32];
    std::cin >> sTemp;
    return 0;
}

vector<double> getRadii() {
        double temp[] = {1};
        vector<double> theVector (temp, temp + sizeof(temp) / sizeof(temp
            [0]));
        return theVector;
}

int doubleI()
{
        double thetai = 10*M_PI/180;
        double theta = 10*M_PI/180;
        double phi = 180*M_PI/180;

    Double_Interaction_BRDF_Model model;
        model.init();

        model.AskUser();
        vector<double> a = getRadii();

        //dielectric_function theIndex;
        //theIndex.read("SilicaRefractiveIndex.txt");
        //dielectric_function theIndex2;
        //theIndex2.read("water.txt");

        //Free_Space_Scatterer_Ptr spherePtr = "MieScatterer";

        //model.set_scatterer(spherePtr);
        //model.get_scatterer()->set_parameter("sphere",theIndex);
        //model.get_scatterer()->set_parameter("coating",theIndex2);
```

```
        //model.get_scatterer()->set_parameter("thickness",0.001);

        vector<double> v;
        double startWN = 900;
        double endWN = 1100;

        for (double i=startWN;i<=endWN;i+=2) {
                v.push_back(i);
        }

        ofstream myfile;
        myfile.open("outputFile0.csv");

        for (int j = 0; j<a.size(); j++) {
                model.get_scatterer()->set_parameter("radius",a[j]);
                model.set_distance(a[j]);

                myfile.close();
                string filename = string("outputFile");
                filename += to_string(j);
                filename += ".csv";
                myfile.open(filename.c_str());

                cout << endl << a[j] << endl;

                for (int i=0; i<v.size(); i++) {

                        model.set_lambda(10000/v[i]);

                        JonesMatrix theJones = model.JonesDSC(thetai,theta,
                            phi,0);
                        complex<double> pp = theJones.PP();
                        complex<double> ps = theJones.PS();
                        complex<double> sp = theJones.SP();
                        complex<double> ss = theJones.SS();

                        myfile <<
                        v[i] << "," <<
                        real(pp) << "," << imag(pp) << "," <<
                        real(ps) << "," << imag(ps) << "," <<
                        real(sp) << "," << imag(sp) << "," <<
                        real(ss) << "," << imag(ss) << endl;
                }
        }

        myfile.close();

        std::cout << "Enter something to exit\n";
    char sTemp[32];
    std::cin >> sTemp;
    return 0;
}

int main(int argv,char** argc)
{
```

```
        int blank = doubleI();
        return 0;
}
```

A.3 Hapke IMSA

The following Matlab function calculates the BRDF using the Hapke IMSA model.

```
function output = hapkeIMSA(w,u,u0,g,xi)
    output = zeros(1,length(w));
    for ii = 1:length(w)
        output(ii) = w(ii)/4/pi*u0/(u0+u)*(henyeyG(g,xi(ii)) + H(u0,w(ii))*
            H(u,w(ii)) - 1);
    end
end

function output = H(u,w)
    g = sqrt(1-w);
    r0 = (1-g)/(1+g);
    output = (1-w*u*(r0+(1-2*r0*u)/2*log((1+u)/u)))^(-1);
end

function output = henyeyG(g,xi)
    output = (1-xi^2)./(1+2*xi*cos(g)+xi^2).^(3/2);
end
```

A.4 Single-Scatter Albedo

The following Matlab function calculates the single-scatter albedo using the model specified by the variable *model*.

```
function [w xi] = determineAlbedo(v,N,a,n0,model)
    %n0 = number fraction of particles such that sum(n0) = 1
    w = zeros(1,length(v));
    xi = zeros(1,length(v));

    if strcmp(model,'Mie')
        vi = 4/3*pi*a.^3;
        ni = n0./vi;
        n = sum(ni);
        meanSigma = sum(ni*pi.*a.^2)/n;

        for ii = 1:length(v)
            disp(ii);

            S = 0;
            E = 0;
            A = 0;
```

```
        xi1 = 0;
        for jj = 1:length(a)
            x = 2*pi*v(ii)*a(jj);
            result = Mie(N(ii),x);
            Stemp = result(2);
            Etemp = result(1);
            Atemp = result(3);
            xiTemp = result(5);
            S = S+Stemp*ni(jj)*pi*a(jj)^2;
            E = E+Etemp*ni(jj)*pi*a(jj)^2;
            A = A+Atemp*ni(jj)*pi*a(jj)^2;
            xi1 = xi1+xiTemp*ni(jj)*pi*a(jj)^2;
        end
        xi(ii) = xi1/n/meanSigma;
        w(ii) = S/E;
    end
end

if strcmp(model,'isoMie')
    vi = 4/3*pi*a.^3;
    ni = n0./vi;

    for ii = 1:length(v)
        disp(ii);

        S = 0;
        E = 0;
        A = 0;
        for jj = 1:length(a)
            x = 2*pi*v(ii)*a(jj);
            result = Mie(N(ii),x);
            Stemp = result(2);
            Etemp = result(1);
            Atemp = result(3);
            xiTemp = result(5);
            w1 = Stemp/Etemp;
            Stemp = Atemp*(1-xiTemp^2)*w1/(1-w1);
            Etemp = Stemp+Atemp;
            S = S+Stemp*ni(jj)*pi*a(jj)^2;
            E = E+Etemp*ni(jj)*pi*a(jj)^2;
            A = A+Atemp*ni(jj)*pi*a(jj)^2;
        end
        w(ii) = S/E;
    end
end

if strcmp(model,'smallParticle')
    vi = 4/3*pi*a.^3;
    ni = n0./vi;

    S = zeros(1,length(v));
    A = zeros(1,length(v));
    for ii = 1:length(a)
        [cabs,qabs,csca,qsca] = bohrenSphere(v,N,a(ii));
        S = S + csca*ni(ii);
```

```
        A = A + cabs*ni(ii);
    end
    w = S./(S+A);
end

if strcmp(model,'equivalentSlabSphere')
    vi = 4/3*pi*a.^3;
    ni = n0./vi;
    n = sum(ni);
    meanSigma = sum(ni*pi.*a.^2)/n;
    theta = linspace(0,pi/2,1000);
    dtheta = theta(2)-theta(1);
    for ii = 1:length(v)
        disp(ii);

        nr = real(N(ii));
        alpha = 4*pi*v(ii)*imag(N(ii));
        S = 0;
        A = 0;
        xi1 = 0;
        for jj = 1:length(a)
            D = 2*a(jj);
            R = singleSurfaceReflectance(1,N(ii),theta,2);
            Se = 2*sum(R.*cos(theta).*sin(theta))*dtheta;
            Si = Se;
            Theta = 2*nr^2/(alpha*D)^2*(exp(-alpha*D*sqrt(abs(1-1/nr^2)
                ))*(1+alpha*D*sqrt(abs(1-1/nr^2)))-exp(-alpha*D)*(1+
                alpha*D));
            Qs = Se + (1-Se)*(1-Si)/(1-Si*Theta)*Theta;
            Qa = 1 - Qs;
            dQs = Se + (1-Se)*(1-Si)/(1+Si*Theta)*(-Theta);
            rfb = (Qs-dQs)/(Qs+dQs);
            if rfb <= 0
                xiTemp = -0.99999;
            else
                rfb3 = rfb^(1/3);
                xiTemp = (rfb3-1)/(rfb3+1);
            end
            S = S+Qs*ni(jj)*pi*a(jj)^2;
            A = A+Qa*ni(jj)*pi*a(jj)^2;
            xi1 = xi1 + xiTemp*ni(jj)*pi*a(jj)^2;
        end
        xi(ii) = xi1/n/meanSigma;
        w(ii) = S/(S+A);
    end
end

if strcmp(model,'equivalentSlabExponential')
    vi = 4/3*pi*a.^3;
    ni = n0./vi;
    n = sum(ni);
    meanSigma = sum(ni*pi.*a.^2)/n;
    theta = linspace(0,pi/2,1000);
    dtheta = theta(2)-theta(1);
    for ii = 1:length(v)
```

```
        alpha = 4*pi*v(ii)*imag(N(ii));
        S = 0;
        A = 0;
        xi1 = 0;
        for jj = 1:length(a)
            D = 2*a(jj);
            Re = singleSurfaceReflectance(1,N(ii),theta,2);
            Ri = singleSurfaceReflectance(N(ii),1,theta,2);
            Se = 2*sum(Re.*cos(theta).*sin(theta))*dtheta;
            Si = 2*sum(Ri.*cos(theta).*sin(theta))*dtheta;
            Theta = exp(-alpha*0.9*D);
            Qs = Se + (1-Se)*(1-Si)/(1-Si*Theta)*Theta;
            Qa = 1 - Qs;
            dQs = Se + (1-Se)*(1-Si)/(1+Si*Theta)*(-Theta);
            rfb = (Qs-dQs)/(Qs+dQs);
            if rfb < 0
                xiTemp = -0.99999;
            else
                rfb3 = rfb^(1/3);
                xiTemp = (rfb3-1)/(rfb3+1);
            end
            S = S+Qs*ni(jj)*pi*a(jj)^2;
            A = A+Qa*ni(jj)*pi*a(jj)^2;
            xi1 = xi1 + xiTemp*ni(jj)*pi*a(jj)^2;
        end
        xi(ii) = xi1/n/meanSigma;
        w(ii) = S/(S+A);
    end
end

if strcmp(model,'equivalentSlabMelamed')
    vi = 4/3*pi*a.^3;
    ni = n0./vi;
    n = sum(ni);
    meanSigma = sum(ni*pi.*a.^2)/n;
    theta = linspace(0,pi/2,1000);
    dtheta = theta(2)-theta(1);
    for ii = 1:length(v)
        alpha = 4*pi*v(ii)*imag(N(ii));
        S = 0;
        A = 0;
        xi1 = 0;
        for jj = 1:length(a)
            D = 2*a(jj);
            Re = singleSurfaceReflectance(1,N(ii),theta,2);
            Ri = singleSurfaceReflectance(N(ii),1,theta,2);
            Se = 2*sum(Re.*cos(theta).*sin(theta))*dtheta;
            Si = 2*sum(Ri.*cos(theta).*sin(theta))*dtheta;
            Theta = 2/(alpha*0.9*D)^2*(1-exp(-alpha*D)*(1+alpha*0.9*D))
                ;
            Qs = Se + (1-Se)*(1-Si)/(1-Si*Theta)*Theta;
            Qa = 1 - Qs;
            dQs = Se + (1-Se)*(1-Si)/(1+Si*Theta)*(-Theta);
            rfb = (Qs-dQs)/(Qs+dQs);
```

```
                if rfb < 0
                    xiTemp = -0.99999;
                else
                    rfb3 = rfb^(1/3);
                    xiTemp = (rfb3-1)/(rfb3+1);
                end
                S = S+Qs*ni(jj)*pi*a(jj)^2;
                A = A+Qa*ni(jj)*pi*a(jj)^2;
                xi1 = xi1 + xiTemp*ni(jj)*pi*a(jj)^2;
            end
            xi(ii) = xi1/n/meanSigma;
            w(ii) = S/(S+A);
        end
    end

end
```

A.5 Monte Carlo

The following Matlab function performs the Monte Carlo simulation described in Section 4.5.

```
function output = monteCarloSimulation4(I,S,A,xi)
    %finalux, finaluy, finaluz: direction cosines of emitted direction
    %finalW: the intensity of the emitted rays
    %multipleFactor: the factor due to russian roulette
    %pathLengths: the total path length of each ray
    %numberScatterEvents: the number of scatter events each ray experiences
    %depths: a list of depths
    %intensity: the intensity at each depth in depths
    %realTheta: list of emitted angles
    %r: the BRDF at each emitted angle

    %prepare cumulative probability function for angle
    theta = linspace(0,pi,10000);
    p = henyeyG(pi-theta,xi);
    p = p.*sin(theta);
    p = p./sum(p);
    pcum = zeros(1,length(p));
    for ii = 1:length(pcum)
        pcum(ii) = sum(p(1:ii));
    end
    pcum(end-1) = (pcum(end)+pcum(end-2))/2;

    eta = rand(1,19000000);
    randTheta = interp1(pcum,theta,eta);
    ltheta = length(randTheta);

    numberOfPhotons = 10000000;
    maxScatterEvents = 1000;
    finalux = zeros(1,numberOfPhotons);
    finaluy = zeros(1,numberOfPhotons);
```

```
finaluz = zeros(1,numberOfPhotons);
finalW = zeros(1,numberOfPhotons);
pathLengths = zeros(1,numberOfPhotons);
numberScatterEvents = zeros(1,numberOfPhotons);
depthMax = 100;
depths = linspace(0,depthMax,100);
dz = depths(2)-depths(1);
intensities = zeros(1,length(depths));
multipleFactor = ones(1,numberOfPhotons);
for ii = 1:numberOfPhotons
    if mod(ii,100) == 0
        disp(ii);
    end
    x = 0;
    y = 0;
    z = 0;
    uxp = sin(I);
    uyp = 0;
    uzp = cos(I);
    W = 1;
    tempIntensities = zeros(1,length(depths));
    notDone = true;
    while notDone
        ux = uxp;
        uy = uyp;
        uz = uzp;
        eta = rand();
        s = -log(eta)/(S+A);
        if (z+uz*s) < 0
            s = (-z-uz*s)/s;
            z = 0;
            notDone = false;
        else
            x = x + ux*s;
            y = y + uy*s;
            z = z + uz*s;
            numberScatterEvents(ii) = numberScatterEvents(ii) + 1;
            W = W*S/(S+A);
        end
        pathLengths(ii) = pathLengths(ii) + s;

        if z <= depthMax

                z2 = z;
                z1 = z-uz*s;
                intensity = W*s;
                if z1 > z2
                    temp = z2;
                    z2 = z1;
                    z1 = temp;
                end
                tempVals1 = depths + dz - z1;
                tempVals1(tempVals1 < 0) = -1;
                tempVals1(tempVals1 > dz) = dz;
                tempVals1 = tempVals1 - dz/2;
```

```
                    tempVals2 = z2 - depths;
                    tempVals2(tempVals2 < 0) = -1;
                    tempVals2(tempVals2 > dz) = dz;
                    tempVals2 = tempVals2 - dz/2;
                    tempVals = tempVals1 + tempVals2;
                    tempVals(tempVals < 0) = 0;
                    tempVals = tempVals/sum(tempVals);
                    tempIntensities = tempIntensities + tempVals*intensity;

                end

                if numberScatterEvents(ii) > maxScatterEvents
                    notDone = false;
                    W = 0;
                else
                    theTheta = randTheta(ceil(rand()*ltheta));
                    [uxp,uyp,uzp] = getNewDirection(ux,uy,uz,theTheta);
                end
            end
            tempIntensities = tempIntensities/pathLengths(ii);
            intensities = intensities + tempIntensities;
            finalux(ii) = ux;
            finaluy(ii) = uy;
            finaluz(ii) = uz;
            finalW(ii) = W;
        end

        theta = acos(-finaluz);
        realTheta = linspace(0,pi/2-0.01,100);
        realW = zeros(1,length(realTheta));
        for ii = 1:length(theta)
            [a b] = min(abs(realTheta-theta(ii)));
            realW(b) = realW(b) + finalW(ii);
        end
        realW = realW./sin(realTheta)./cos(realTheta)/2/pi/(realTheta(2)-
            realTheta(1))/numberOfPhotons;

        temp = struct;temp.finaluz = finaluz;temp.finaluy = finaluy;temp.
            finalux = finalux;temp.finalW = finalW;temp.pathLengths =
            pathLengths;temp.numberScatterEvents = numberScatterEvents;temp.
            depths = depths;temp.intensities = intensities;temp.multipleFactor =
             multipleFactor;temp.r = realW;temp.realTheta = realTheta;
        output = temp;
    end
```

A.6 Speckle

The following Matlab function simulates a speckle image given a distance to the object plane D, an f-number fn, a wavenumber v, and a matrix of electric field amplitudes in the object plane s.

```
function output = calculateSpeckleImage(D,fn,f,v,s)
```

```
    %D = distance
    %fn = f number
    %f = focal length
    %v = wavenumber
    %s = scatter image
    %assumes 1 cm image plane
    zi = 1/(1/f-1/D);
    lp = fftshift(fft2(s));
    r0 = f/fn/2*v/zi*1;
    bandpass = createCircle(zeros(1000),r0);
    lp2 = lp.*bandpass;
    final = ifft2(ifftshift(lp2));
    final = abs(final).^2;
    output = final;
end
```

Bibliography

[1] Hinkov, Borislave et al. “Broad band tunable quantum cascade lasers for stand-off detection of explosives.” Proc. of SPIE Vol. 7484, 748406.

[2] Fuchs, Frank; Hinkov, Borislav; Hugger, Stefan; Kaster, Jan M.; Aidam, Rolf; Bronner, Wolfgang; Kohler, Klaus; Yang, Quankui; Rademacher, Sven; Degreif, Kai; Schnurer, Frank; and Schweikert, Wenka. “Imaging stand-off detection of explosives using tunable MIR quantum cascade lasers.” *Quantum Sensing and Nanophotonic Devices VII*, Proc. of SPIE Vol. 7608, 760809, 2010.

[3] Suter, Jonathan et al. “Angle resolved scattering spectroscopy of explosives using an external cavity quantum cascade laser.” Proc. of SPIE Vol. 8268, 8268R.

[4] Hapke, Bruce. *Theory of Reflectance and Emittance Spectroscopy*. Cambridge Books Online, 2012.

[5] Manolakis, D.,M. Pieper, E. Truslow, T. Cooley, M. Brueggeman, and S. Lipson, ”The remarkable success of adaptive cosine estimator in hyperspectral target recognition,” Proc. SPIE 8743, 874302 (2012).

[6] Goodman, J.W. *Speckle Phenomena in Optics: Theory and Applications*. Ben Roberts and Company, 2007.

[7] Matzler, Christian. “Matlab Functions for Mie Scattering and Absorption.” June 2002.

[8] Bohren, Craig F. and Donald R. Huffman. *Absorption and Scattering of Light by Small Particles*. John Wiley and Sons, Inc., 1983.

[9] Alieva 1993.

[10] Bobbert, P.A. and Vlieger, J. “Light Scattering by a Sphere on a Substrate.” Physica 137A (1986) 209-242.

[11] Goyal, Anish et al. ”Time Evolution of the Long-Wave Infrared (LWIR) Signatures of VX Simulant on Environmental Surfaces.” *MIT Lincoln Laboratory Report*, 26 March 2012.

[12] Hansen, G.B. "Calculation of single-scattering albedos: Comparison of Mie Results with Hapke approximations." *Icarus* 203 (2009) 672-676.

[13] Dainty, J. C. *Laser Speckle and Related Phenomena*. Springer-Verlag Berlin Heidelberg, 1975.

[14] Berg, Matthew J.; Sorenson, C.M.; and Chakrabarti, A. "A new explanation of the extinction paradox." *US Army Research*. Paper 110.

[15] Dunayevskiy, Ilya; Tsekoun, Alexei; Prasanna, Manu; Go, Rowel; and Patel, C. Kumar N. "High-sensitivity detection of triacetate triperoxide (TATP) and its precursor acetone." *Applied Optics*, Vol. 46, No. 25, 1 September 2007.

[16] Fuchs, Frank; Jarvis, Jan Phillip; Hugger, Stefan; Kinzer, Michel; Yang, Quankui; Bronner, Wolfgang; Driad, Rachid; and Aidam, Rolf. "Imaging Standoff Detection of Explosives by Diffuse Reflectance IR Laser Spectroscopy." Future Security 2012, CCIS 318, pp. 388-399, 2012.

[17] Goodman, J.W. "Statistical Properties of Laser Speckle Patterns." Stanford Electronic Laboratories Technical Report No. 2303-1, December 1963.

[18] Goyal, A.K.; Myers, T.; Spencer, M.; Kunz, R.; Park, S.; Tipton, B; Kelly, M; Holthoff, E. L.; Farrel, M. E.; and Pellegrino, P.M. "Active infrared hyperspectral imaging of solid particles on surfaces." *SPIE Defense Security and Sensing*, Baltimore 2013.

[19] Goyal, A.K.; Myers, T.; Wang, C. A.; Kelly, M.; Tyrrell, B.; Gokden, B.; Sanchez, A.; Turner, G.; and Capasso, F. "Active hyperspectral imaging using a quantum cascade laser (QCL) array and a digital-pixel focal plane array (DFPA) camera." *Optics Express* (submitted) 2014.

[20] Hapke, Bruce. "Bidirectional Reflectance Spectroscopy: 1. Theory." *Journal of Geophysical Research*, Vol. 86, No. B4, Pages 3039-3054, April 10, 1981.

[21] Herbst, Johannes; Hildenbrand, Jurgen; Wolkenstein, Jurgen; and Lambrecht, Armin. "TATP and TNT detection by mid-infrared transmission spectroscopy." *Infrared Technology and Applications XXXV*, Proc. of SPIE Vol. 7298, 72983W.

[22] Liang, Shunlin and Townshend, John R. G. "A Modified Hapke Model for Soil Bidirectional Reflectance." Remote Sens. Environ. 55:1-10 (1996).

[23] Maradudin, A.A. and Michel, T. "The Transverse Correlation Length for Randomly Rough Surfaces." *Journal of Statistical Physics*, Vol. 58, Nos. 3/4, 1990.

[24] Mishchenko, Michael I. "Gustav Mie and the fundamental concept of electromagnetic scattering by particles: A perspective." *Journal of Quantitative Spectroscopy and Radiative Transfer* 110 (2009) 1210-1222.

[25] Phillips, M. C. and Ho, N. "Infrared hyperspectral imaging using a broadly tunable external cavity quantum cascade laser and microbolometer focal plane array." Opt. Express 16, 5708-5714 (2008).

[26] Thelen, Alfred. *Design of Optical Interference Coatings*. McGraw-Hill, Inc., 1989.

[27] Troccoli, M. et al. "Quantum Cascade Lasers and Their Applications in Molecular Recognition." Royal Society of Chemistry 2013.